REVIEW

Check for updates

Two-photon polymerization-assisted 3D laser nanoprinting: from fundamentals to modern applications

Ibrahim Boudene [ID] [a] and Yahya Bougdid [ID] *[bc]

A key aspiration of modern science is to precisely control and arrange matter on a nanoscale level, creating 3D microstructures with specific functions. Microstereolithography technology has significantly pushed the frontiers of this aspiration, facilitating the manufacture of microdevices that offer innovative solutions in various sectors. Among different microstereolithography techniques, 3D laser nanoprinting based on two-photon polymerization (2PP) has emerged as a powerful tool for addressing complex challenges in a variety of scientific and industrial fields, with capabilities far exceeding those of traditional lithography techniques. Its unique ability to fabricate complex 3D microdevices with nanometer-scale precision has opened up new applications in a wide range of fields, including optics, electronics, and medicine. However, 2PP technology is still in its infancy, and many challenges have yet to be overcome, underscoring the need for further research and development to maximize the potential of 2PP lithography (2PL). This review aims to provide a comprehensive overview of 2PL, highlighting its fundamental background, experimental aspects, and various functional photoresists. Moreover, we review the fundamental principles underlying the exceptional spatial resolution and the key factors enhancing the feature resolution and surface accuracy of 2PP-printed microstructures. Finally, we explore diverse potential applications of 2PL across various disciplines and share current challenges, innovations, and future prospects in this field.

1. Introduction

Micro- and nano-manufacturing technologies have great potential to drive the global technology economy and shape international diplomacy. This has led to growing global geopolitical competition surrounding the control of these technologies, as in the case of ASML (Advanced Semiconductor Materials Lithography) and TSMC (Taiwan Semiconductor Manufacturing Company), which manufacture the most sophisticated nanoscale semiconductor chips for use by the world's leading electronics companies, including Apple and Intel.[1] Stereolithography (SLA) has emerged as a powerful tool in the field of micro/nanofabrication, enabling leading companies like IBM (International Business Machines) corporation and TSMC to leverage this technology to dominate the global electronic microchips manufacturing industry. However, although these traditional microstereolithography techniques achieve unprecedented resolution,

they are generally limited to planar (2D) manufacturing and often require specialized equipment and extreme conditions similar to those required for electron beam lithography (EBL) and extreme UV (EUV) lithography.[2] Therefore, there is a growing need for new nanofabrication techniques that offer complex 3D structural versatility and precise design capabilities (*i.e.*, accuracy in spatial resolution), all with attainable equipment and conditions. Two-photon polymerization-based nanoprinting, also known as "two-photon lithography (2PL)" or "3D laser nanoprinting" or "two photon 3D printing", has established itself as a promising and cost-effective nanofabrication alternative, enabling the creation of complex 3D microstructures with exceptional precision and high spatial resolution in 3D.[3–6] Moreover, 2PL technology is not primarily limited to the electronics sector, as is the case with traditional microstereolithography techniques, and its scope of applications could include other potential sectors, such as microrobotics, optics, and medicine.[7–10] Interestingly, although still in its early stages of growth compared to other techniques, 3D laser nanoprinting has the potential to revolutionize the field of nanoscale printing and perhaps reshape the global technology economy in the near future.

Historically, the first attempt to print a 3D microstructure using 2PL dates back to 1997 by Kawata's group.[11] They fabricated a 3D spiral microstructure of 6 μm and 1.3 μm in

[a] Laboratory of Advanced Materials and Process Engineering, Faculty of Sciences, Ibn Tofail University, Kenitra 14000, Morocco

[b] Center for Research and Education in Optics and Lasers (CREOL), The College of Optics and Photonics, University of Central Florida, Orlando, Florida 32816, USA. E-mail: yahya.bougdid@ucf.edu

[c] Department of Mechanical and Aerospace Engineering, College of Engineering and Computer Science, University of Central Florida, Orlando, Florida 32816, USA

This journal is © The Royal Society of Chemistry 2025

J. Mater. Chem. C, 2025, **13**, 18597–18630 | **18597**

diameter and width, respectively, representing the smallest 3D microstructure fabricated at that time without stacking 2D structures. In 2001, the same team[12] took 2PL from microscale to nanoscale printing by successfully fabricating a functional 3D micro-oscillator of 300 nm in diameter with 120 nm feature sizes, corresponding to around $\lambda/6.5$ resolution, far below the diffraction limit resolution. Since then, a significant amount of research has been invested in exploring the capabilities of 2PP in 3D nanoprinting, enabling the fabrication of functional 3D microdevices at even smaller scales, while also offering advantages in terms of speed, flexibility, stability, and low manufacturing cost.[3,5,13–15] The advancement of 2PL is mainly attributed to ultrafast laser technology, particularly femtosecond (Fs) lasers, which generate ultra-high peak power with extremely short pulse durations.[10,16] Indeed, when the intense peak power of these Fs lasers is tightly focused (*i.e.*, spatially localized) using an objective lens (OL), they can selectively induce polymerization at precise points within the resin volume, *i.e.*, voxels. The induced polymerization is triggered by the two-photon absorption (2PA) process – a nonlinear optical (NLO) effect that enables the near-simultaneous absorption of two photons.[16,17]

A key aspect of 2PL is the optimization of laser processing parameters to enhance both resolution and throughput. Accordingly, adjustments of factors such as laser pulse duration, repetition rate, laser dose, exposure time, and irradiation wavelength significantly influence the size and precision of the printed features.[18–21] The development of advanced photoresists has also contributed to the improvements of 2PL technology, offering a diversity of applications, high stability, and high-precision manufacturing. In this context, researchers have developed biocompatible, stimuli-responsive materials designed to polymerize more precisely under specific conditions, enabling the fabrication of intricate microdevices for a variety of biomedical applications, including tissue engineering, microfluidics, and drug delivery systems.[22–24] Moreover, hybrid materials combining organic and inorganic elements have been developed, opening up new possibilities for creating functional microstructures suitable for use as optical and photonic microdevices.[25–27] Fig. 1 summarizes some of the cutting-edge functional applications in various fields achieved by 3D laser lithography using different photoresist materials. Further advancements in 2PL have come from improvements in the optical system. For instance, the adoption of the multiple laser foci (focal points) approach and integration of Galvo-scanners with piezoelectric stages (PZTs) have facilitated mass production and faster manufacturing.[28,29] Other enhancements to the 2PL system have been specifically implemented to improve resolution by reducing the size of printed voxels. For instance, the use of shorter laser wavelengths coupled with finely tuned Fs pulses, *e.g.*, two-photon deep UV (DUV) polymerization, has enabled a significant reduction in voxel size and limited heat diffusion (lower intensities), resulting in high 2PL resolution.[30,31] Hybrid approaches, combining 2PL with other techniques such as one-photon lithography and nanoimprinting, have also played a crucial role in accelerating and scaling up production while maintaining high structural complexity.[32,33] Also, the recent introduction of computational tools, such as machine learning algorithms and process simulations, to assist Fs machining has proven to be a promising approach to tackle several 2PL challenges, including accuracy, speed, and reproducibility.[34–37] As a result, 2PL is increasingly being used in precision-demanding fields due to its high accuracy and superior reproducibility. Moreover, although printing speed currently limits its suitability for rapid and mass manufacturing, ongoing efforts are effectively tackling this challenge through advanced strategies such as AI-guided printing optimization, new photoresist formulations, and parallelization techniques, making 2PL more viable for high-throughput applications too. These innovations collectively demonstrate how 2PL is becoming a versatile and scalable method for 3D nanoprinting, positioning it as a powerful tool for the future of micro-manufacturing.[6,8,15]

Ibrahim Boudene

Ibrahim Boudene is a PhD researcher at Ibn Tofail University, Morocco. He received his MSc degree from Mohammed V University, graduating with the highest honors in both his MSc and BSc cohorts. During his collaboration with the Center of Optics & Photonics at Mohammed VI Polytechnic University (UM6P)-MAScIR Foundation, he developed expertise in laser nanofabrication of 2D/3D micro/nanostructures, along with plasmonic nanomaterials. He was one of the first pioneering PhD students on the African continent to create 2D/3D microstructures using nanolithography technology. Ibrahim is currently expanding his expertise to include inorganic nanostructures aimed at advancing energy generation and storage technologies.

Yahya Bougdid

Yahya Bougdid earned his PhD in Photonics and nanotechnology from Mohammed V University in Rabat, Morocco. He is currently a researcher at CREOL and CECS, University of Central Florida, USA. His doctoral research focused on two-photon 3D-nanoprinting, where he played a pioneering role in establishing 2PP-printing technology in Morocco. He was the first PhD student able to fabricate 3D-microscale structures using this techno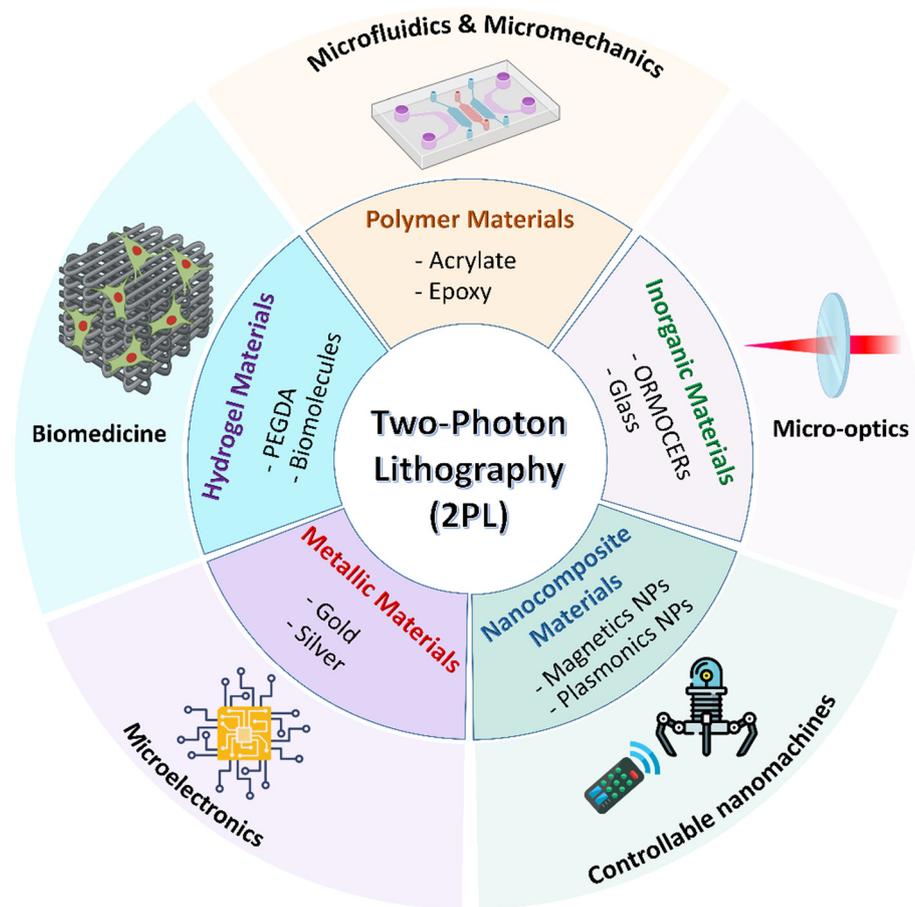logy on the African continent. His current research areas include laser additive manufacturing, laser sintering, laser doping of silicon carbide, nano-electrospray laser deposition, and the fabrication of nanoparticle-based thin patterns/films for applications in solar cells and optical coating.

18598 | *J. Mater. Chem. C*, 2025, **13**, 18597–18630

This journal is © The Royal Society of Chemistry 2025

Fig. 1 Schematic diagram illustrating various classes of photoresist materials used in 2PL and their related applications. The icons were created in BioRender, Bougdid, Y. (2025), **BioRender.com/4ep2rdw**. The nanomachine icon made by Freepik from **www.flaticon.com**.

All the above-mentioned improvements and advancements have qualified 2PL to fabricate a wide variety of complex and functional 3D microdevices, which were previously impossible to manufacture using traditional microfabrication techniques. Some typical examples include micromechanical systems,[38,39] photonic crystals,[40,41] microscale robots,[42] micro-optical components,[43,44] micro-needles,[15] and drug delivery micro-carriers.[45] These 2PP-printed microdevices have unlocked potential applications in various disciplines.[7,46,47] For example, Hu and coworkers[48] have taken advantage of 2PL's high precision and robustness to fabricate 3D programmable-shape soft micromachines (*i.e.*, microactuators) that are promising for future soft micromechanics applications. Staufer *et al.*[49] employed 2PL to print microfluidic systems, enabling the production of precise, interconnected fluidic networks ideal for lab-on-a-chip applications such as biosensing and chemical analysis. In the realm of robotics, Suter's team[50] used 2PL to manufacture microrobots, underscoring the technique's capacity for producing highly functional and miniaturized robots that can be utilized in diverse fields, from medical diagnostics to environmental monitoring. In photonics, Deubel *et al.*[51] harnessed the power of 2PL to design nanoscale 3D photonic crystals, highlighting their potential application in telecommunication. In micro/nano-optics, Gissibl *et al.*[43] used 2PL to manufacture complex,

ultracompact multi-lens objectives that showed unprecedented optical performance and high-quality imaging, promising a new generation of miniature optical instruments, including endoscopic instruments, detectors, imaging systems, and *in vivo* optical fibers. In the field of biomedicine, Ovsianikov *et al.*[52] leveraged 2PL to manufacture biomedical scaffolds, emphasizing its utility in tissue engineering, where precise control over scaffold structures is critical for successful cell growth and regeneration. Furthermore, Bozuyuk and coworkers[45] utilized 2PL to fabricate remotely controllable personalized drug delivery systems, a key innovation for precision medicine, where customized drug formulations can be delivered to specific locations within the body with high accuracy. Currently, several companies, including Nanoscribe GmbH[53] and Multiphoton Optics GmbH,[54] offer commercial 2PL systems that further enable rapid, reproducible, and precise fabrication of submicrometer-scale devices. Such commercialized 2PP printing systems have become very popular and useful for fabricating complex, functional 3D microstructures in a variety of research fields, including electronics, photonics and biomedicine. A timeline of major milestones and developments in 2PL technology is given in Fig. 2.

This review provides a comprehensive overview of 2PP-assisting 3D printing, first describing the fundamentals of the 2PA process (Section 2) and the principles of 2PP nanoprinting

This journal is © The Royal Society of Chemistry 2025

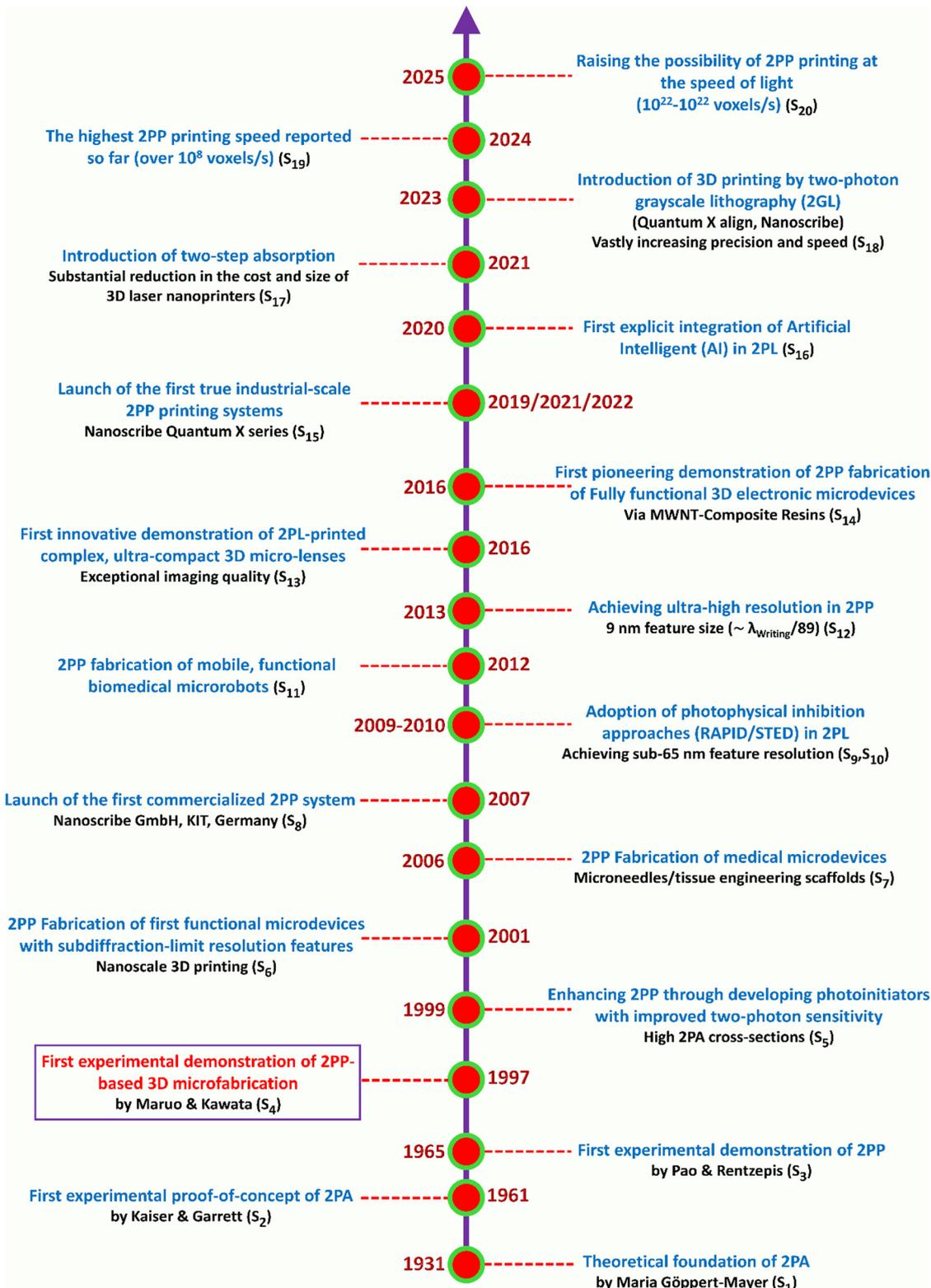*J. Mater. Chem. C*, 2025, **13**, 18597–18630 | **18599**

Fig. 2 Timeline of major milestones and developments in 2PL technology. S1 (ref. 55), S2 (ref. 56), S3 (ref. 57), S4 (ref. 11), S5 (ref. 58), S6 (ref. 12), S7 (ref. 59), S8 (ref. 53), S9 (ref. 60), S10 (ref. 61), S11 (ref. 62), S12 (ref. 63), S13 (ref. 43), S14 (ref. 64), S15 (ref. 65), S16 (ref. 66), S17 (ref. 67), S18 (ref. 68), S19 (ref. 69), and S20 (ref. 70).

(Section 3). Then, in the fourth section, various photosensitive materials used in 2PL are discussed, illustrating some exciting examples of functional 3D microstructures fabricated on different photoresists. 2PL experimental instrumentation is also reported in Section 4. Section 5 delves into the theoretical principles underlying the exceptional feature resolution achieved with 2PL

18600 | *J. Mater. Chem. C*, 2025, **13**, 18597–18630

This journal is © The Royal Society of Chemistry 2025

and examines various strategies for improving the resolution and surface accuracy of 2PP-printed microstructures. Moreover, Section 6 presents a selection of advanced practical 2PP applications in micro-optics and imaging, microelectronics/optoelectronics, and biomedicine. Section 7 explores both major challenges and promising innovations for industrial-scale manufacturing and widespread commercial adoption of 2PL. Finally, we conclude the review by summarizing the key concepts and prospects of 2PP-based 3D printing.

2. Fundamentals of 2PA

2.1. Spectroscopic mechanism of 2PA

The concept of 2PA was theoretically predicted by M. G. Mayer in 1931.[55] However, it was not observed experimentally until the invention of lasers a few years later.[56] The process of 2PA can be conceptualized as a non-resonant Raman scattering process; both techniques use non-resonant photons to excite the molecule to a virtual excited state. However, in Raman scattering, the electron is relaxed from this virtual state to the lower electronic state, emitting a second non-resonant photon. Conversely, in the 2PA process, a second non-resonant photon is also absorbed, and the electron continues to the higher electronic state, corresponding to the sum of the frequencies of the two absorbed photons.

A crucial condition for inducing the 2PA process is exposing photosensitive molecules to very intense bursts of light, so that these molecules absorb two photons almost at once and excite the electron to a higher electronic state.[71,72] A simplified Jablonski diagram demonstrating the spectroscopic mechanisms of 1PA and 2PA processes is shown in Fig. 3a. In the 1PA process, a single photon with sufficient energy ($h\nu$) excites the molecule from its ground electronic state (E_0) to its higher excited state energy (E_1). Conversely, in 2PA, two photons of half-energy ($h\nu/2$ each) are almost simultaneously absorbed by the molecule within an extremely short timeframe (~ 1 fs).

Although each individual photon has insufficient energy to reach E_1, their combined energy is sufficient to promote the electronic transition ($E_0 \rightarrow E_1$) that is mediated by a virtual/intermediate state. Following both the 1PA and 2PA excitations, *i.e.*, 1PE and 2PE respectively, the molecule undergoes a non-radiative relaxation process, subsequently followed by the spontaneous emission of a lower energy fluorescent photon (λ_{em}).[16,72,73]

2PA is regarded as another way of unlocking a molecule's excited state; instead of using a single, high-powered photon of short wavelength, 2PA allows two lower-energy photons to combine and act as a single photon, performing the same electronic excitation.[71] Therefore, because of the distinct selection rules governing excitation induced by 2PA compared to 1PA, the 2PA process has been widely recognized as a highly valuable tool in spectroscopy.[75,76] If the energy of the two photons is identical, 2PA is called a degenerate process; otherwise, it is called a non-degenerate process. Most applications employ the degenerate 2PA process because of the simplicity of the experimental setup, especially for 2PL.[16,17]

2.2. Theory of 2PA

2PA is a nonlinear (NL) phenomenon that offers many advantages over the linear process of 1PA, paving the way to a number of potential techniques and applications, such as two-photon fluorescence 3D data storage,[77] two-photon fluorescence microscopy,[78] and two-photon 3D printing.[11] A key advantage of 2PA over 1PA is that the laser beam can penetrate deeper into the photosensitive medium without being absorbed by the surrounding material along the laser path, and absorption only occurs selectively at the laser focal spot (LFS), where the intensity is high enough to induce 2PE. In contrast, for 1PA, where the absorbing medium is excited by resonant photons, absorption occurs along the entire laser beam path. Webb's group[74] has demonstrated this effect by exciting a fluorescent medium with resonant (1PA) and non-resonant (2PA) photons.
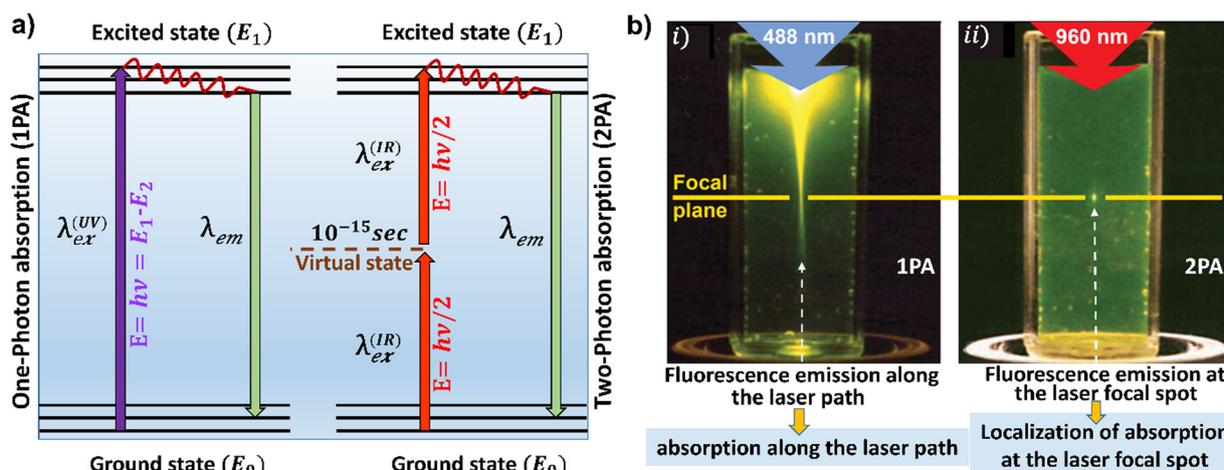

Fig. 3 (a) Jablonski diagram illustrating 1PA and 2PA mechanisms. (b) (i) Localization of absorption along the beam path by focused 488 nm laser excitation, corresponding to 1PE, and (ii) localization of absorption at the focal plane using focused 960 nm pulsed laser excitation, corresponding to 2PE. The absorption is probed by the intense yellow fluorescence emission. (b) Reproduced with permission.[74] Copyright 2003, Springer Nature.

This journal is © The Royal Society of Chemistry 2025

J. Mater. Chem. C, 2025, **13**, 18597–18630 | **18601**

Notably, in 1PA, yellow fluorescent photons were emitted over almost the entire laser beam path (Fig. 3bi); meanwhile, in 2PA, fluorescence emission occurred only at the LFS, indicating that the absorption is confined to an infinitely small volume inside the medium (Fig. 3bii).[74]

Accordingly, the most common photosensitive resins used in 2PL are nearly transparent to NIR light, allowing the IR Fs laser beam to penetrate deep into the resin and only polymerize around the LFS (Fig. 4aii). In contrast, in 1PA, the excitation light (*i.e.*, UV and visible light) is strongly absorbed by the resin, and the entire laser beam path is solidified by polymerization from the resin surface to the bottom (Fig. 4ai). Wegner and coworkers[79] further demonstrated the efficiency of 2PP over 1PP using the tail-accumulation model.

Remarkably, although they used a larger 2PP voxel size (λ_1 = 800 nm) than that of 1PP (λ_2 = 400 nm), they demonstrated that the 2PP-printed microstructures are far better than that printed with 1PP, particularly at high accumulation exposure doses (Fig. 4b). This effect is attributed to the tail of the LFS, which has a significant absorption effect on the resin in linear absorption (1PA). For example, considering that the tail of the LFS in 1PA absorbs 1% relative to the maximum focal intensity per exposure, after 100 exposures, the accumulated intensity at this LFS tail would reach 100% of the focal maximum according to the accumulation model. Meanwhile, in 2PA, the same LFS tail intensity, which corresponds here to 0.1% due to the NL effect, will reach only 1% relative to the focal maximum after 100 exposures, which is effectively negligible.[13] Consequently, 2PA enables polymerization to be limited only to a tightly localized volume corresponding to the diffraction-limited LFS, *i.e.*, voxel (the 3D equivalent of a 2D pixel). This high-level control of the laser distribution density in 2PP allows for achieving high spatial accuracy, enabling the creation of precise and complex 3D microstructures, as reported elsewhere.[19,43,46,80,81] In the following, we discuss the optical technology systems used to generate high peak laser intensities to enable the 2PA process, then explore the absorption properties of 2PA materials and demonstrate the NL dependence of the absorption probability on 2PE intensity.

2.2.1. Ultrashort pulsed lasers for 2PA

Using lasers with extremely short and high-intensity energy pulses is crucial for making the 2PA process efficient enough for practical applications. Fs lasers are particularly well suited to triggering an efficient 2PE thanks to their ability to generate ultra-high peak power with very short pulse durations at high repetition rates.[10,16,82] Fig. 5b illustrates the temporal distribution of photon density in continuous-wave (CW) and pulsed-wave laser modes. While the CW laser emits a continuous, uniform, and low photon density over time, the pulsed Fs laser confines the emitted photons in infinitely small pulses lasting only a few tens of femtoseconds, *e.g.*, 120 fs pulse width, with only 12 ns or shorter between pulses. These pulses generate sufficiently high instantaneous intensity, which is several orders of magnitude higher than that of CW lasers.[14,16] Spatial confinement of photons within a very small region is also achieved utilizing a high-numerical aperture OL, as illustrated in Fig. 5b. Consequently, the high temporal and spatial confinements afforded by pulsed Fs lasers significantly increase the photon density within a small volume, improving the probability of absorbing more than one photon and thus effectively triggering 2PA.

In 2PL, the energy dose required to trigger 2PA and subsequent polymerization can be attained through prolonged exposure to CW IR laser intensity or ultrafast IR laser with high-intensity pulses. However, since they lack the peak intensity required to efficiently trigger 2PA, it is extremely challenging for
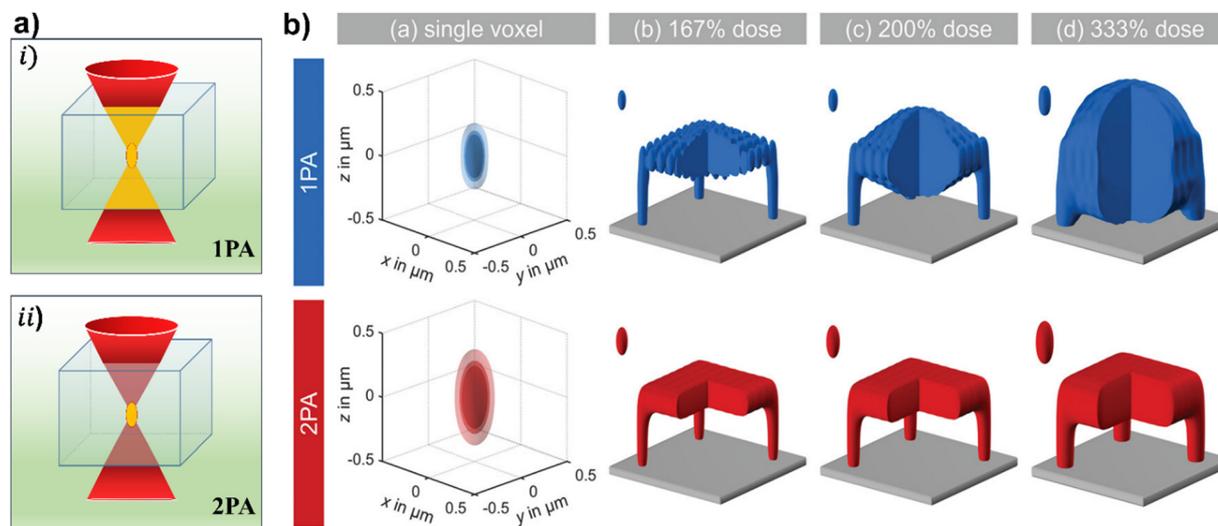

Fig. 4 (a) (i) 1PA induced polymerization (1PP) and (ii) 2PA-induced polymerization inside the photosensitive resin. The yellow regions represent the polymerized areas, while the yellow ellipsoid indicates the LFS, *i.e.*, the voxel. 2PP is spatially confined to the LFS. (b) Illustration of 3D-printed tables by 1PA and 2PA using the tail-accumulation model reported in ref. 65. The 167%, 200%, and 333% values correspond to the accumulated exposure dose used for 1PP and 2PP. The 2PA voxel size is deliberately chosen to be larger than that of 1PA. (b) Reproduced under the terms of the Creative Commons CC-BY License.[79] Copyright 2020, the Authors, Published by Wiley-VCH.
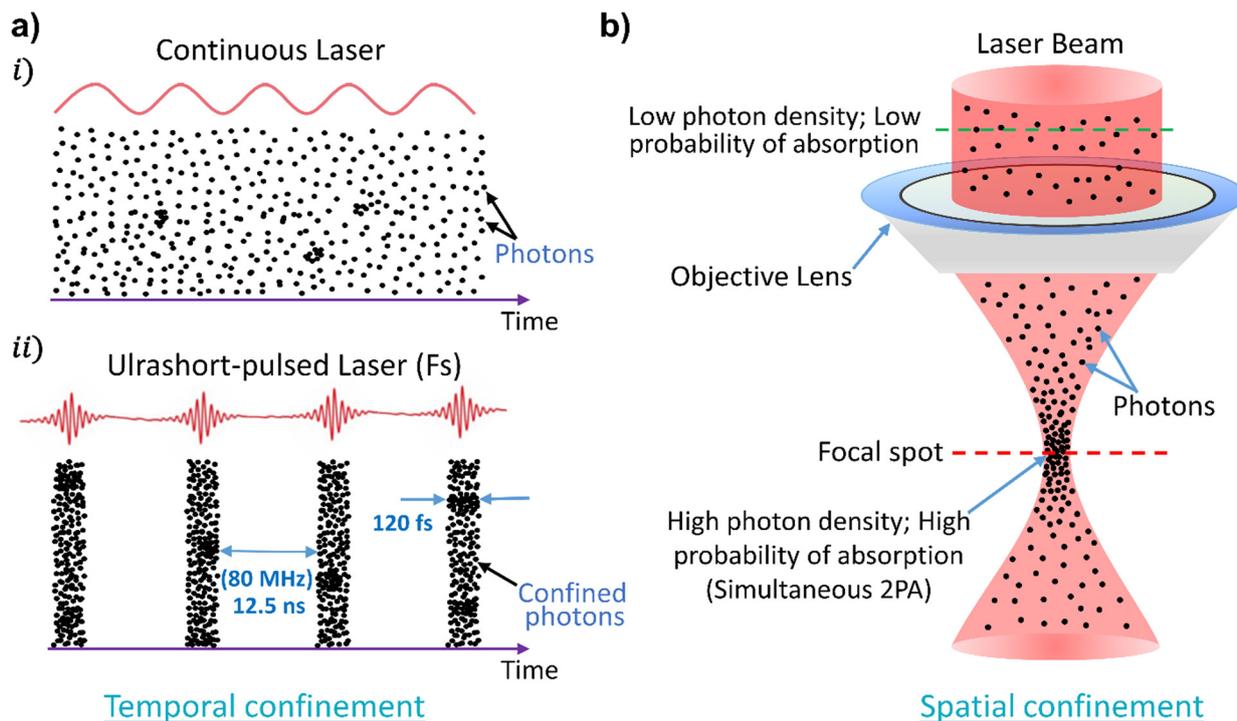
Fig. 5 Schematic illustrations demonstrating the increasing probability of 2PA through temporal and spatial confinement. High temporal confinement cannot be achieved by CW laser, which emits a continuously low photon density over time (ai). In contrast, Fs lasers, which emit high-instantaneous intensity pulses, can achieve high temporal confinement of photons (aii). (b) Spatial confinement of photons within an infinitely small volume (LFS) using a high-numerical OL.

CW IR lasers to induce 2PP. In contrast, 2PA-induced polymerization has been successfully and easily achieved using pulsed IR irradiation under equivalent power energy conditions.[14]

For instance, a pulsed IR laser (*e.g.*, λ = 780 nm) operating at a repetition rate of 80 MHz (80 × 10^6 pulses per s), with 120 fs pulse width and emitting a 1 mW average power, can produce a tiny Gaussian diffraction-limited LFS ($\sim$0.7 μm) with a photon flux density of about 2 × 10^{29} photons per s cm^2 over the pulse duration. This is about 10^5 times higher than the photon flux density delivered by a CW laser ($\sim$2 × 10^{24} photons per s cm^2) under the same excitation conditions. Consequently, ultrafast-pulsed lasers are a crucial key element for triggering 2PP, providing very short and high-instantaneous intensity pulses capable of inducing NL absorption.

2.2.2. 2PA cross-section (σ_2)

Careful choice of the physico-chemical properties of the photosensitive molecules is crucial to achieving a highly efficient 2PE, with a particular focus on materials exhibiting excellent NL absorption properties.[16] The NL absorption properties of photosensitive materials are typically expressed in terms of cross-section (σ_2), which reflects the 2PA probability and efficiency. Considerable efforts and investments have been devoted to investigating the cross-section of 2PA materials, with the aim of developing photosensitive molecules that exhibit significantly enhanced 2PA cross-sections.[58] Interestingly, materials with larger 2PA cross-sections require a very small photon flux density to induce efficient 2PE, enabling the use of low-power, cost-effective

lasers, such as nanosecond (ns) pulsed lasers, in various 2PA-based applications.[83] The 2PA cross-section represents the effective area that a photosensitive molecule reveals for interacting with the incident 2PA-inducing laser beam. Accordingly, the σ_2 of 2PA-molecules is given with units of (GM); 1 GM = 10^{-50} cm^4 s per photon, where the cm^4 unit is the product of two areas, each corresponding to each photon in the 2PA process. Experimentally, the value of σ_2 of 2PA materials is determined by several techniques, such as Z-scan measurements, NL transmission, and two-photon induced fluorescence/phosphorescence.[84,85] Nevertheless, to achieve high 2PP nanoprinting efficiency, 2PA materials must meet a few other chemical and physical requirements, such as high quantum yield, high ablation threshold, and compatibility with the resin mixture (*vide infra*).

2.2.3. Non-linear (NL) behavior of 2PA

NL absorption refers to the NL change in photon flux or intensity as the beam passes through a photosensitive medium. For lower intensities, this effect is not observable, and the rate of absorption varies linearly with laser intensity (I), corresponding to $-\frac{\mathrm{d}I}{\mathrm{d}z} = \alpha I$.[86] However, for sufficiently high instantaneous intensities, the probability for molecules to absorb more than one photon is significantly enhanced, and the absorption rate becomes no longer linear with intensity. In the case of 2PA, the absorption rate becomes proportional to the square of the laser beam intensity (I^2), and it is expressed as: $-\frac{\mathrm{d}I}{\mathrm{d}z} = \beta I^2$,

This journal is © The Royal Society of Chemistry 2025

J. Mater. Chem. C, 2025, **13**, 18597–18630 | **18603**

where β is the 2PA coefficient in NL absorption.[87,88] The value of β is determined by the imaginary part of the third-order susceptibility of the molecule's polarization ($\chi^{(3)}$), which is responsible for the strength of the NL absorption, and is given as follows:[88,89]

$$\beta = \frac{3\pi}{\varepsilon_0 n^2 c \lambda} \mathrm{Im}\left(\chi^{(3)}\right) \qquad (1)$$

where ε_0, n, c, and λ are the vacuum permittivity, the refractive index (RI), the light speed in vacuum, and the incident light wavelength, respectively. Based on the second-order perturbation theory for the interaction of an electromagnetic field with a molecule, the transition probability/rate ($W_T^{(2)}$) between two allowed bands and the 2PA coefficient (β) is expressed as follows:[90]

$$W_T^{(2)} = \frac{\beta I^2}{2\omega} \qquad (2)$$

where $\hbar\omega$ represents the energy of the incident photon. β is commonly used to describe the absorption properties of bulk molecules macroscopically. However, it can be related to the absorption properties of a single molecule, i.e., 2PA cross section (σ_2), by the molecular number density (N_0) (molecules per cm^3). The relationship between both coefficients is given as follows:[88]

$$\beta = \frac{\sigma_2 N_0}{\hbar\omega} \qquad (3)$$

Combining eqn (2) and (3), the transition rate is then expressed in eqn (4) in terms of the absorption of an individual molecule:

$$W_T^{(2)} = \frac{\sigma_2 N_0 I^2}{2\hbar^2 \omega^2} \qquad (4)$$

The quadratic dependence of the molecule's excitation rate on the intensity in eqn (4) clearly demonstrates the NL behavior of absorption at the atomic level, which is consistent with the NL absorption effect observed at the macroscopic level. Because of this higher-order dependence of absorption probability on intensity, near-simultaneous 2PA will only be possible at much higher intensities, thus confining the absorption to the focal point where the intensity is highest. In 2PL, this will enable the fabrication of high-resolution features with sizes comparable to, or even smaller than, the diffraction-limited LFS. The sub-diffraction limit (SDL) resolution of 2PL caused by the NLO absorption will be detailed in Section 5.

3. Fundamentals of two-photon 3D printing

3.1. Polymerization reaction mechanism

Photopolymerization-based lithography has emerged over the past two decades as a powerful technique for fabricating a wide range of 3D microstructures, offering significant potential for various applications.[7,8,47] Its key advantage lies in its ability to produce large-scale, complex microstructures with exceptional resolution through a simple and rapid photochemical reaction.[5,91] Generally, photopolymerization is a photochemical process that uses light to convert liquid or gel-like monomers into solid polymers. This sol–gel conversion process is achieved via a polymerization reaction that is initiated by incorporating photosensitive molecules, such as initiators, into the initial material. Among initiators, there are two popular systems: radical and cationic. This section reports the mechanism of 2PA-assisted radical polymerization. Typically, the process of 2PP begins with the NL absorption of two photons by the photoinitiator (PI), elevating its electrons to the singlet excited state (PI*/S) (Fig. 6a). The energy of these singlet-excited electrons can dissipate through internal conversion (vibrational relaxation or fluorescence emission) or intersystem crossing of electrons to the triplet excited state (PI*/T), i.e., by inversion of electron spin.
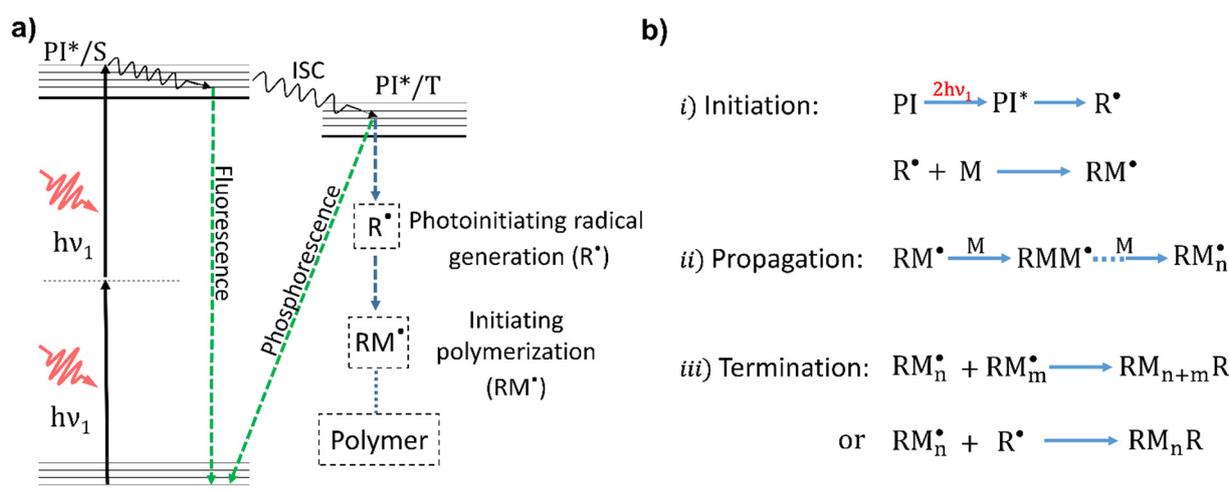

Fig. 6 (a) Jablonski diagram illustrates the energy level transitions induced by 2PA to initiate the polymerization reactions. Among many scenarios, one could lead to the formation of radicals. This involves first a transition of the monomer to the singlet excited state (PI*/S), followed by a transition to the triplet excited state (PI*/T). In this state, the monomer bond can undergo cleavage, generating two separate radicals that initiate polymerization. (b) 2PA-induced polymerization steps that are responsible for the formation of solid polymer. ISC: intersystem crossing; PI: photoinitiator; PI*: excited-state PI; R$^\bullet$: radical; M: monomer.

18604 | J. Mater. Chem. C, 2025, 13, 18597–18630

This journal is © The Royal Society of Chemistry 2025

Triple-excited electrons either convert their energy into radiation energy (phosphorescence) when they return to the singlet ground state, or their excited energy is quenched by other species, such as oxygen molecules.[16,73] If the energy of the triplet state is sufficiently high, another scenario can occur in which bound electrons separate, leading to breaking of the PI's chemical bonds and the generation of reactive radicals. These extremely reactive radicals attack monomer bonds and generate monomer radicals that, in turn, attack additional monomer bonds, thereby promoting the growth of polymer chains through the propagation step. These polymer chains continue to grow until quenched, either by reacting with each other or with other radical species, particularly dissolved oxygen molecules (termination step) (Fig. 6b).[16,73,92]

Photosensitizers with larger cross sections are sometimes incorporated into the photosensitive 2PA materials to improve the excited-electrons population in the PI system by transferring absorbed energy (or excited electrons) to PI molecules.[93] However, PIs with a high excited-electrons population are insufficient to trigger efficient 2PP reaction after excitation; instead, PI molecules must also exhibit high efficiency in generating intermediate radicals (high quantum yield).[16,94]

3.2. Principles of 2PP-assisted 3D nanoprinting

Compared with other nanofabrication techniques, such as two-beam interference lithography,[95,96] EUV[97,98] and EBL,[99] 2PL offers outstanding advantages. In addition to its 3D capability and superior micromachining resolution, it requires no mask, mold, or stamp for fabrication, and its optical setup is quite simple and does not require extreme conditions, such as vacuum or clean room environment. Typically, the 2PP manufacturing process begins with the design of the desired 3D microstructure using computer-aided design (CAD) software. The digital model is then converted into a compatible format, typically a standard tessellation language (STL) file suitable for the computer-controlled printing system. The STL file is further processed by specialized software, which slices the 3D model into a series of layers and generates precise manufacturing instructions. These instructions are transmitted to the laser writing system, which sequentially polymerizes the photosensitive resin layer by layer, enabling the creation of intricate microstructures with high precision. The 2PP writing system typically consists of a laser source, a focusing OL, and a 3D scanning stage. The oil immersion OL, typically of high NA ($\sim$1.4–1.45), is used to precisely focus the laser beam into the resin. The inverted OL focusing configuration is commonly used in 2PL, where a droplet of the resin is deposited on the cover glass substrate, and the laser beam is focused from the bottom. The immersion oil is inserted between the OL and the substrate's back side to reduce aberrations and match the RI, enabling a tightly focused LFS size[100] (see the zoomed-in version in Fig. 10).

2PP scanning systems usually utilize two scanning modes: scanning the laser beam inside the photoresist or scanning the photoresist across the fixed laser beam. In the first mode, a pair of Galvo mirrors is used to monitor the scan of the laser in x- and y-dimensions, and a PZT is used to move the sample up and down in the z-direction. In the second mode, the sample is moved in all three dimensions (XYZ) using a motorized 3D PZT.

The choice of 2PP scanning mode depends on the specific requirements of the fabrication process. On the one hand, the Galvo-scanning system is ideal for fabricating larger structures in a shorter processing time due to its faster scanning speed (several m s^{-1}). However, in this mode, the overall patterning area is small because of the limitations associated with the objective's field of view. On the other hand, although operating at slower speeds than the Galvo systems, the PZT scanning mode is ideal for fabricating large-scale and high-resolution 3D microstructures, as it offers large travel distances (mm to cm) with more precise motion resolution.[3,29] The integration and synchronization of both systems (i.e., 3D PZT/3D linear stage with Galvo mirrors) has also been used in 2PL, providing high velocities, high-resolution features, and large-scale manufacturing.[21,101]

The 2PL system supports two main scanning methods for 3D printing: raster and contour scanning.[9,102] Raster scanning involves scanning the entire volume of the microstructure voxel by voxel, then layer-by-layer, which guarantees high precision but increases processing time (Fig. 7ai). In contrast, the contour method focuses on scanning the surface or contour profile of the structure to fabricate a shell-like 3D microstructure. The liquid resin inside the microstructure is subsequently polymerized after the washing step using a UV light (Fig. 7aii). The latter method significantly reduces processing time and is, therefore, particularly useful for fabricating larger microstructures for which high precision at every point/pattern of the entire structure is not required. During polymerization, the matter state of the polymerized and unpolymerized photoresist becomes different, resulting in a contrast in the RI. This enables real-time monitoring of the 2PP process using a white-light microscope equipped with a lamp, OL, and a CCD camera. After two-photon 3D printing (Fig. 7bi), the unexposed regions of the negative-tone resist (or laser-exposed regions of the positive-tone resist) are washed out using a developer, typically an organic solvent such as ethanol (Fig. 7bii). This step leaves behind a freestanding 3D microstructure on the substrate surface (Fig. 7biii), replicating the initially designed computer model.

4. Materials and methods for 2PL

The versatility and exceptional capabilities of 2PP 3D printing are primarily due to the NLO effects of ultrafast-pulsed lasers and the wide variety of photoresist materials available for 2PL. This section reports the various photoresist materials used in 2PL, and the optical setup required to excite these materials with ultrashort-pulsed lasers to enable 3D manufacturing of microstructures.

4.1. 2PA materials: photopolymerizable resin

Since almost any photosensitive material can be micro-patterned using 2PL, most materials used for 2PP were initially borrowed from conventional lithography techniques, including PI molecules.[11,85] However, recent advancements have led to the development of new 2PA materials specifically designed for 2PL, particularly PI molecules, intending to improve resolution,
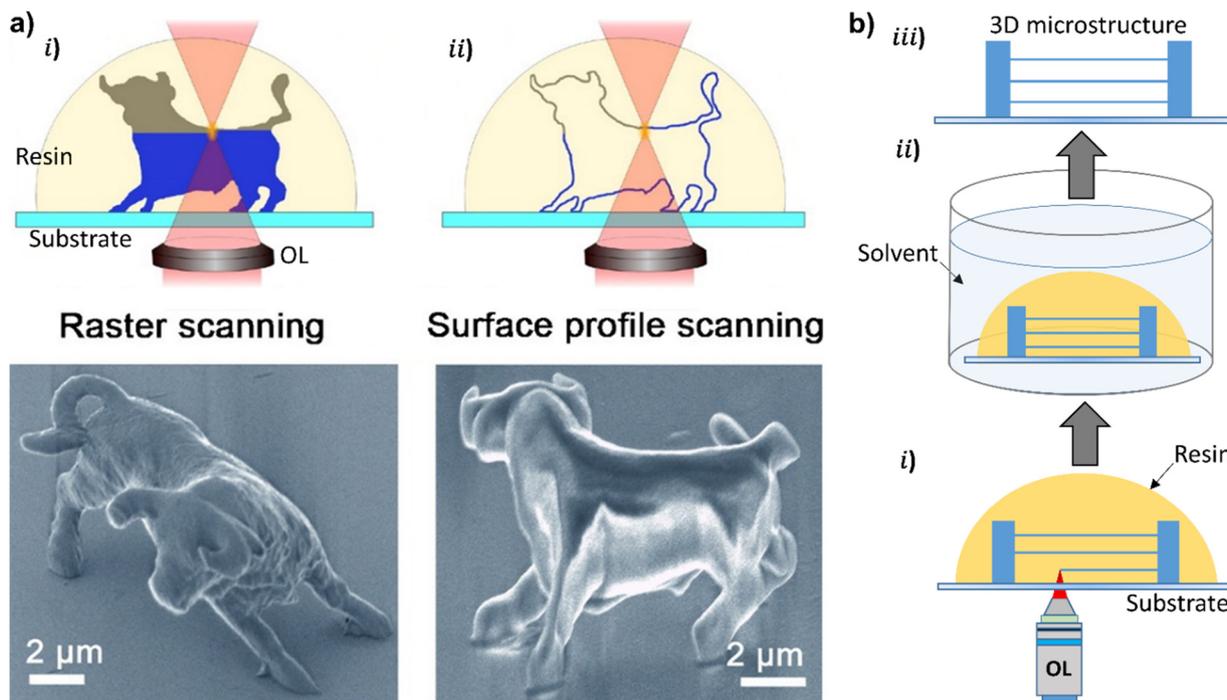
Fig. 7 (a) Schematic illustration for 2PP scanning modes and SEM micrographs of micro-sized 3D-printed bull sculpture fabricated by (i) raster scanning mode (fabrication time: 180 min), and by (ii) surface profile/contour scanning mode followed by UV light irradiation for solidifying the inner liquid resin (fabrication time: 13 min). (b) Schematic representation of the 2PP steps for fabricating 3D microstructures. First, the desired 3D microstructure is laser-printed inside the resin (i). Next, the unpolymerized/unsolidified resin is washed away by an organic solvent (ii), leaving only the polymerized microstructure on the cover glass surface (iii). (a) Reproduced from ref. 5, with permission. Originally published in ref. 12. Copyright 2001, the Authors, Springer Nature.

stability, and speed and broaden the range of potential applications.[73,103] 2PA materials are generally composed of two main components: PIs and monomers. PIs are molecules capable of simultaneously absorbing two photons and generating active species, such as radicals and cations, which are responsible for initiating the polymerization photoreaction. Monomers serve as building blocks for the printed microstructures, forming the main skeleton when activated by the excited PIs. Additional components could also be incorporated into the resin to enhance the microstructures' characteristics and performance. Crosslinkers, for example, can increase the photoresist's viscosity and improve the stability and strength of the printed microstructures. Photosensitizers can be added to enhance the generation of active species. Inhibitors can also be added to control the polymerization process and improve the printing resolution. Finally, solvents are used to dissolve the various components to obtain a homogeneous resin mixture.

Photoresists used for 2PL must meet several requirements to ensure fast, efficient, and high-quality printing.[94] Typically, a photoresist must be transparent at the laser-printing wavelength. The monomers should have a fast-curing speed to guarantee rapid polymerization and, therefore, a fast-manufacturing process. The crosslinked material must be resistant to certain solvents to ensure the survival of polymerized microstructures during the development stage. The ablation threshold of the resin should be sufficiently high in relation to its 2PP intensity threshold. Finally, the photoresist must have an optimized viscosity to prevent the

deformation of microstructures during the printing process. Generally, 2PP photoresists can be broadly classified into positive and negative photoresists. While positive photoresists can be useful for applications requiring large 3D porous structures,[104] such as microfluidic devices,[49] negative photoresists are often preferred due to their versatility for most advanced and functional applications.[3,105]

Acrylate-based resins (*e.g.*, IP photoresists) and epoxy-based resins (*e.g.*, SU-8 series) are the most widely commercialized negative photoresist materials for 2PL. Both resins are organic-based materials but have distinct polymerization mechanisms; acrylate monomers undergo radical polymerization, while epoxy monomers polymerize *via* a cationic mechanism. SU-8 is widely commercialized for 2PL due to its high printing precision, Vis-IR transparency, and mechanical strength.[106,107] However, compared to resins based on radical polymerization, SU-8 has several limitations, including multi-step processes and the need for post-baking after laser exposure to initiate polymerization. Additionally, SU-8 resins exhibit lower printing resolution and longer processing times compared to radical polymerization-based resins.

Acrylate- and methacrylate (MA)-based resins, which undergo radical polymerization, have significantly advanced 2PL research thanks to their exceptional properties. They offer fast curing speeds, Vis-to-IR transparency, low shrinkage, and excellent mechanical properties.[46,108] Fig. 8a illustrates the absorption spectrum of a resin composed of methyl MA (MMA) monomers.

18606 | *J. Mater. Chem. C*, 2025, **13**, 18597–18630

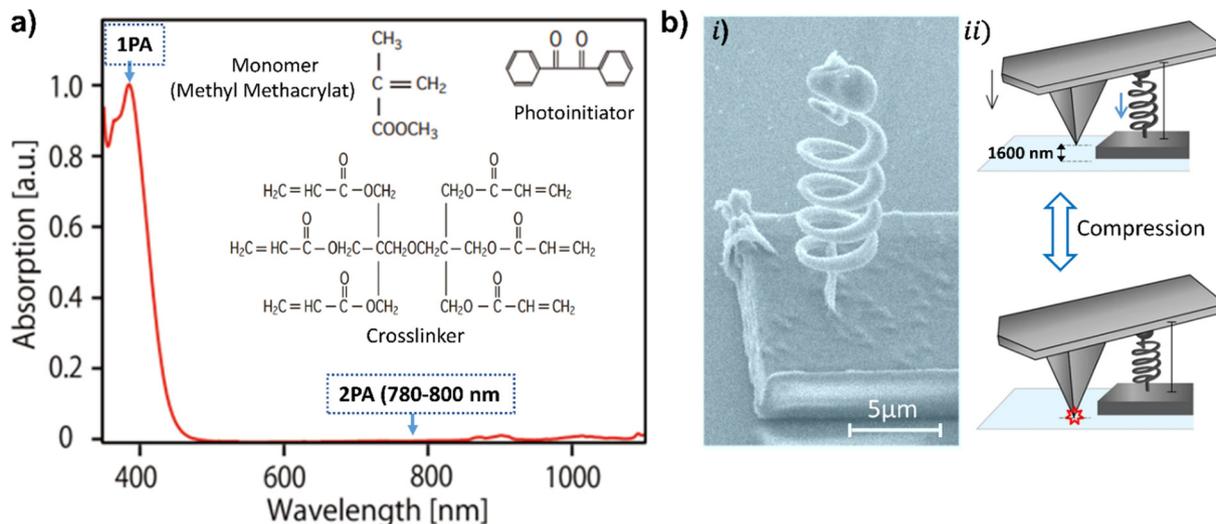This journal is © The Royal Society of Chemistry 2025

Fig. 8 (a) Absorption spectrum of MMA resin. The components of the resin are shown in the inset. (b) (i) SEM micrograph of a freestanding 2PP-printed nano-sized coil spring fabricated using the MMA resin shown in (a). (ii) Scheme illustrating a compression test performed on the μ-coil spring using AFM. (a) and (b) Reproduced under the terms of the Creative Commons License CC BY 4.0.[109] Copyright 2015, the Authors, published by Springer Nature.

The MMA resin exhibits a maximum band absorption in the UV region, but near-zero absorption in the visible and NIR regions, especially at the typical 2PP writing wavelengths (*i.e.*, typically 780–800 nm). Ushiba *et al.*[109] demonstrated the superior nanomechanical properties of polymerized MMA-based resins by fabricating a well-standing nano-sized coil spring using 2PL (Fig. 8b). Compression tests, performed using the atomic force microscopy (AFM) technique, revealed that the micro coil spring exhibits excellent mechanical responses to the applied forces, following the same linearity as macroscopic springs (Hook's law). SCR500 (JSR, Japan),[12] Nopcocure 800 (San Nopco, Japan)[110] and Sartomer photoresist products (Sartomer Corporation, USA), *e.g.*, SR348,[111] are among the acrylate/MA-based resins most widely used in 2PL.

Over the past decade, many companies specializing in 2PP printing have released advanced manufacturing systems with a wide range of optimized photoresist materials, *i.e.*, mostly consisting of acrylate/MA-based photoresists. Among these companies, Nanoscribe GmbH (Karlsruhe, Germany), with its Photonic Professional GT system, has gained popularity among researchers due to its advanced capabilities[112] and high-quality photoresists (*e.g.*, IP-series resists).[113] Their well-optimized photoresists enabled the fabrication of large-scale, ultra-complex, high-resolution, and multifunctional devices with exceptional speed and efficiency.[81,114] For example, Fig. 9a demonstrates a complex, upscale, and high-resolution 3D chiral structure fabricated using Nanoscribe's IP-Dip photoresist. This structure comprises over 100 000 3D unit cells, representing perhaps the largest high-resolution microstructure, including the highest number of 2PP-printed voxels (∼300 billion voxels).[81] The versatility of acrylate resins also offers the advantage of being easily functionalized with other compounds, which significantly broadens their range of applications. For example, polyethylene glycol (PEG) molecules can be functionalized with acrylate groups (*e.g.*, PEGDA) to create hydrogel materials with potential biomedical engineering applications, such as

tissue engineering scaffolds.[115] Furthermore, the functionalization of biomolecules such as proteins (*e.g.*, bovine serum albumin (BSA)) with acrylate or other biocompatible groups can extend the utility of these materials for the fabrication of smart biomimetic 3D microenvironments and advanced biomedical microdevices.[24,116]

To improve the properties and performance of 2PP printed microstructures, hybridizing inorganic matrices with organic groups has become a common practice. For example, organically modified ceramics (ORMOCERs, Microresist Technologies, Germany), composed of an inorganic backbone (–Si–O–Si–) and functionalized with organic species such as acrylates, are hybrid materials that have gained widespread recognition in two photon 3D printing, notably due to their ability to produce high-resolution 3D microstructures with enhanced mechanical properties and finely tunable optical properties (*e.g.*, tunable RI). These exceptional properties of ORMOCERs make them particularly attractive for a wide range of optical and photonic applications.[25,117] Nanocomposites are another promising class of photoresist materials that have gained increasing importance in 2PL. These materials combine the properties of the organic polymer matrix with the exceptional properties of nanoparticles (NPs) such as carbon nanotubes (CNTs), quantum dots (QDs), and plasmonic NPs. Incorporating these NPs into photoresists offers the possibility of introducing or enhancing the optical, electrical, mechanical, and magnetic properties of the printed microstructures.[64,118–122] For example, by incorporating Fe_3O_4 NPs in MA resins, Sun *et al.*[123] successfully fabricated a microturbine whose motion is remotely controlled by an external magnetic force (Fig. 9b).

Shape memory polymers (SMPs) are stimuli-responsive materials capable of reversible shape transformations when triggered by stimuli such as light, heat, magnetic fields, or electrical signals. In 2PL, SMP-based photoresists enable the fabrication of dynamic microstructures like microactuators and biomedical
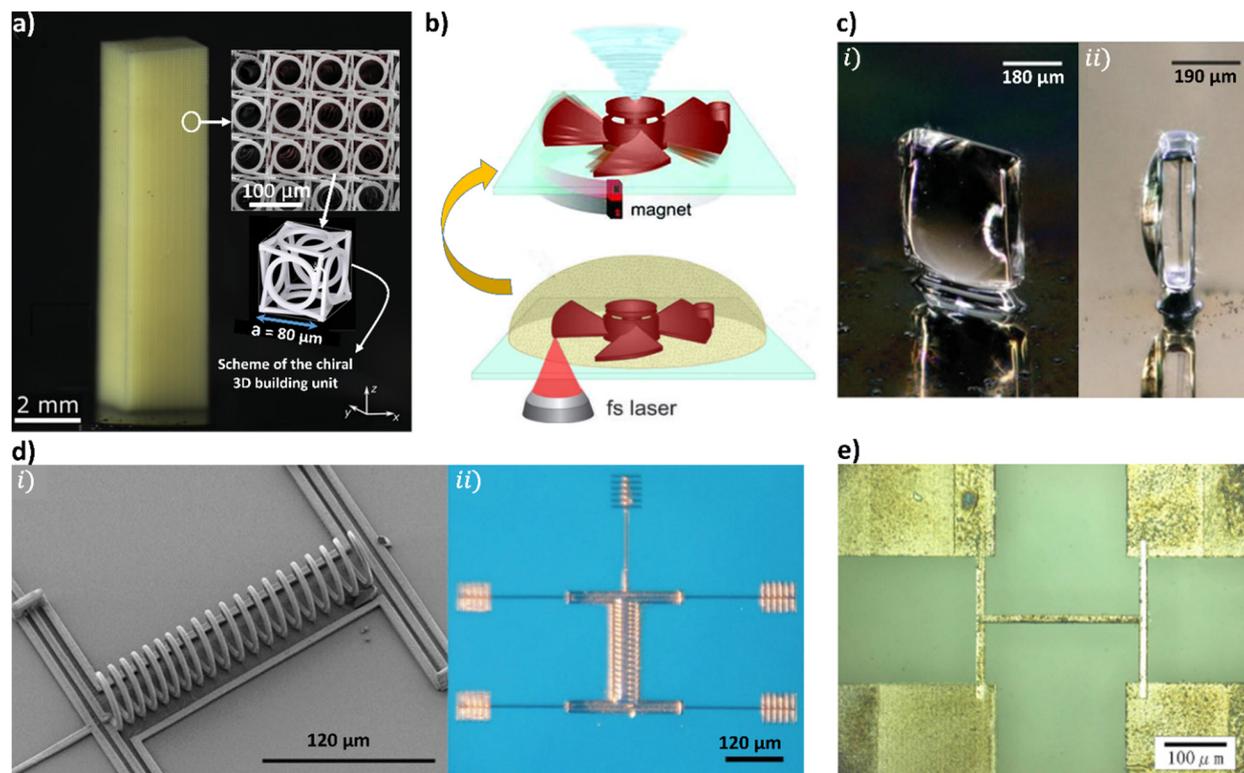
This journal is © The Royal Society of Chemistry 2025

J. Mater. Chem. C, 2025, **13**, 18597–18630 | **18607**

Fig. 9 (a) Optical photograph of a 3D chiral structure fabricated using Nanoscribe's IP-Dip photoresist. This 3D structure contains around 10^5 3D unit cells. Reproduced with modifications under the terms of the Creative Commons CC-BY License.[81] Copyright 2020, the Authors, Wiley-VCH. (b) Magnetically remote-controlled micro-turbine fabricated using a nanocomposite MA-based resin doped with Fe_3O_4 NPs. Reproduced (with modifications) with permission.[123] Copyright 2010, Wiley-VCH. (c) Pure FSG microlens manufactured by 2PL followed by a post-sintering process; (i) upright view and (ii) side view. Reproduced under the terms of the Creative Commons CC-BY License.[44] Copyright 2021, the Authors, Wiley-VCH. (d) (i) SEM micrograph and (ii) optical micrograph of a copper-coated acrylic-based micro-inductor. Reproduced under the terms of the Creative Commons License CC BY 4.0.[129] Copyright 2007, Elsevier. (e) Silver (Ag) wire of approximately 12 μm diameter fabricated using a Fs laser through a two-photon photoreduction procedure. The Ag wire was connected to four gold (Au) electrodes for conductivity measurement. The results showed that the fabricated Ag wire is electrically conductive. Reproduced with permission.[131] Copyright 2008, Optica Publishing Group.

devices.[124] SMP composites, enhanced with functional materials, offer improved mechanical strength, remote actuation, and large recoverable deformation. Their integration with 2PL is promising for developing adaptive, reconfigurable microsystems in fields such as soft robotics, flexible electronics, and 4D printing.[124,125] These advancements bridge the gap between static printed structures and intelligent microsystems capable of shape adaptation and functional transformation on demand, thus expanding the scope of smart materials in 2PP-enabled applications. A comprehensive review of SMPs and their composites, covering mechanisms, materials, and diverse applications, is provided by Xia *et al.* in ref. 124.

2PL also enables the fabrication of pure inorganic 3D microstructures with SDL resolution. One approach involves dispersing inorganic NPs within an organic photoresist, followed by a post-sintering process to remove the organic matrix.[119,126] Kotz and coworkers[44] reported the fabrication of highly efficient fused silica glass (FSG) using a nanocomposite material consisting of amorphous SiO_2 NPs (40 nm size) embedded in a photopolymerizable resin matrix. The transition from the fabricated nanocomposite microstructure to the pure FSG was achieved through a two-step post-processing procedure. First, the polymer

matrix was removed by heat treatment at 600 °C, and then the microstructure was thermally sintered at 1300 °C to form a dense FSG microstructure. This approach enabled them to fabricate transparent FSG-based microlenses with an optical transmittance of 92% and a perfectly smooth surface with less than 6 nm roughness (Fig. 9c). Furthermore, a pure metallic 2D/3D microstructure can be successfully fabricated with 2PL using the aforementioned post-sintering approach or other approaches.[127,128] One approach is to coat the metal onto the fabricated organic microstructure (Fig. 9d).[129,130] Another promising approach consists of directly fabricating metallic microstructures from a metallic aqueous salt solution using a process known as two-photon reduction.[131,132]

The fabrication of metallic 2D/3D microstructures has great potential for applications in industrial sectors, specifically in microelectronics and plasmonics metamaterials.[6,133,134] The choice of PI in 2PL is crucial for achieving efficient, compatible, and precise 3D microstructures.[16,94] Accordingly, efficient PIs should exhibit the following characteristics: (i) a high 2PA σ_2 to efficiently absorb two photons simultaneously, (ii) a high quantum yield to efficiently generate reactive species (radicals/cations), (iii) good solubility and compatibility with the resin

18608 | *J. Mater. Chem. C*, 2025, **13**, 18597–18630

This journal is © The Royal Society of Chemistry 2025

mixture, and (iv) an optimal processing window as PIs must have a low polymerization threshold and a high damage threshold. For biological/biomedical applications, the PI should be biocompatible, non-toxic, and biodegradable in order to ensure its safety for biological systems. Some typical commercially available PIs commonly used in 2PL include Irgacure-369,[108] Lucirin TPO-L,[135] Rose Bengal,[136] iodonium and sulfonium salts,[137] and (E)-stilbene systems.[58] All these PIs offer a wide range of properties and can be selected based on the specific requirements of the fabrication process and the applications of the printed microdevices.

4.2. Optical setup for 2PL

The 2PL optical setup can vary depending on specific application requirements, but the basic components remain common. The 2PL setup shown in Fig. 10 can be divided into three main parts: (i) an irradiation source and beam adjusting components; (ii) a laser beam-focusing component (i.e., OL) and a real-time monitoring system; and (iii) a computer controller and a 3D scanning system. The irradiation source generally consists of an ultra-pulsed laser system, typically a mode-locked Ti:sapphire Fs laser, which can produce pulses lasting tens to hundreds of fs at a repetition rate of the order of 80 MHz and with a tunable wavelength range between 700 nm and 1000 nm. An attenuator is mounted directly after the laser source to control the laser power and adjust it to the required intensity to induce 2PP reaction. Next, the attenuated laser beam is expanded and collimated using a pair of lenses to fill the back aperture of the OL. A pinhole is carefully positioned at the focal point of the first lens to spatially filter the beam. Expanding the laser beam before the OL also helps to control the beam's divergence, which is critical for achieving high precision and focus. A mechanical shutter is used to control exposure times during 2PP printing. A dichroic mirror, reflective for NIR and transparent for visible light, directs the laser beam toward the

back of the OL. In the second part of the 2PP printing system, the OL focuses the laser beam onto the sample to pattern the desired 3D microstructure. The printed microstructure is monitored in real-time using a lamp light that passes through a low-pass filter and the sample. The image of the microstructure taken by the lamp light is magnified by the OL and focused onto the CCD camera to visualize the real-time printing. The real-time monitoring is very useful for ensuring the success of the printing process, and for adjusting the z-position of the LFS to ensure appropriate anchoring of the printed structures to the substrate. The final part of the system involves a computer control workstation that converts the desired 3D model into a high-resolution 3D scanning motion of the PZT. The PZT precisely coordinates the desired structure within the resin in XYZ directions. The computer control also manages the ON/OFF state of the laser beam through a fast mechanical shutter.

5. Feature resolution in 2PL

The feature resolution in conventional optical lithography has historically been restricted by the diffraction limit of light, as described by Abbe's formula (eqn (5)).[138] This formula establishes a direct relationship between the object's resolution and the wavelength of light. To overcome the resolution limitations associated with light wavelength, researchers have progressively adopted shorter wavelengths for micro/nanofabrication, transitioning from UV to deep UV (DUV), and now EUV lithography with a light source wavelength as short as λ = 13.5 nm.[139] However, while traditional lithography techniques have focused on reducing the laser wavelength, 2PL offers a unique approach, which is based on the NLO effect, to significantly improve feature resolution regardless of the laser wavelength. In fact, by taking advantage of NLO and threshold effects, 2PL can achieve SDL resolution even using longer IR wavelengths.
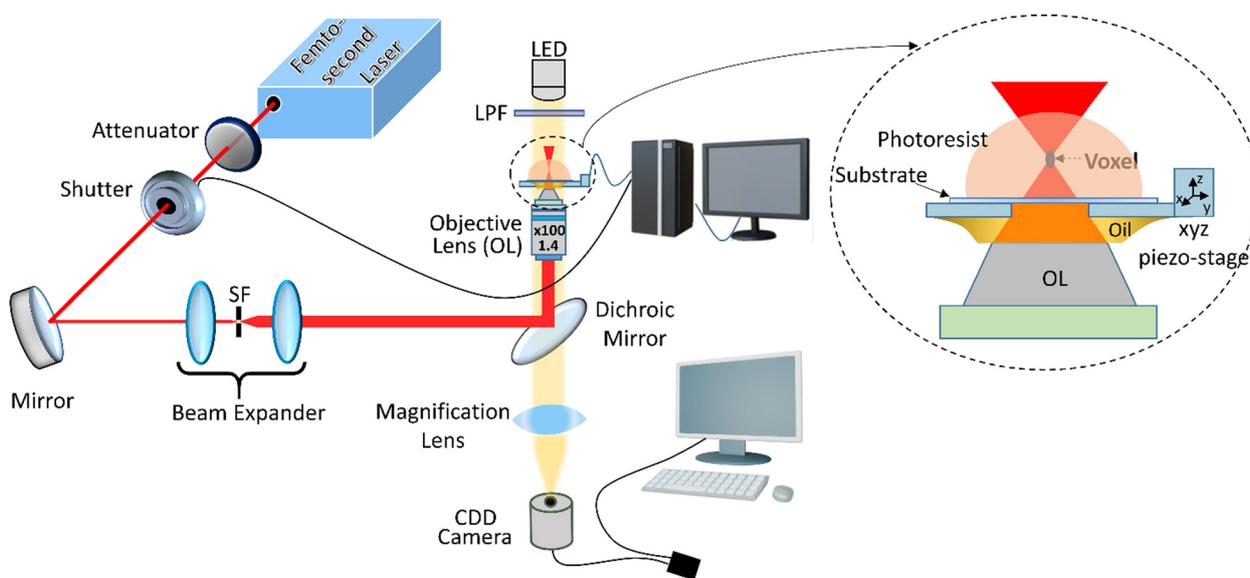

Fig. 10 Experimental setup for 2PP-assisted 3D nanoprinting. The setup is equipped with a three-axis PZT and inverted OL focusing configurations. SF: spatial filter, LPF: low pass filter.

This journal is © The Royal Society of Chemistry 2025

J. Mater. Chem. C, 2025, **13**, 18597–18630 | **18609**

This breakthrough enables 3D printing of microstructures with unprecedented precision and detail.[12] It is noteworthy that resolution refers typically to the minimum distance between two objects that can be distinguished as separate entities by an OL. However, 2PP resolution refers mostly to the smallest printed feature size, which corresponds to the dimension of the polymerized 3D voxel size, *i.e.*, feature resolution.

5.1. NLO effect in 2PP Printing

According to Abbe's theory,[138,140] the diffraction limit represents the theoretical maximum resolution or the smallest LFS size that an optical instrument, such as an OL, can achieve. The minimum achievable LFS size, as defined by

Abbe's criterion, is given by:

$$r = \frac{\lambda}{2NA} \quad (5)$$

here, r denotes the minimum radius of the LFS, λ is the laser wavelength, and NA is the numerical aperture of the focusing OL. NA is expressed as $NA = n\sin(\theta)$, where n represents the RI of the medium, and θ the half maximum convergence angle. For pulsed lasers with a Gaussian beam profile, the minimum

radius of the LFS (beam waist, w_0) can be approximated as follows:

$$w_0 = \frac{\lambda}{\pi NA} \quad (6)$$

w_0 described in eqn (6) is defined as the lateral distance from the center of the LFS, where the intensity is at its maximum, to the point where the intensity decreases to approximately 37% (or $1/e$) of its peak value. eqn (6) works well in a linear absorption regime, *i.e.*, 1PA. However, 2PP can achieve an even smaller w_0 due to the NL 2PA process. The NL effect associated with 2PA is illustrated in Fig. 11a, where the squared light intensity (SLI) distribution of the Gaussian beam is sharper and narrower compared to the standard Gaussian distribution in 1PA. The 2PA Gaussian profile was found to be reduced by a factor of $\sqrt{2}$ compared to the 1PA Gaussian profile. This allows decreasing w_0 by a factor of $\sqrt{2}$, and, consequently, improves the 2PP resolution.[141,142]

5.2. Polymerization threshold effect in 2PL

In addition to the NLO effect, the polymerization threshold effect also plays a crucial role in enhancing 2PP feature
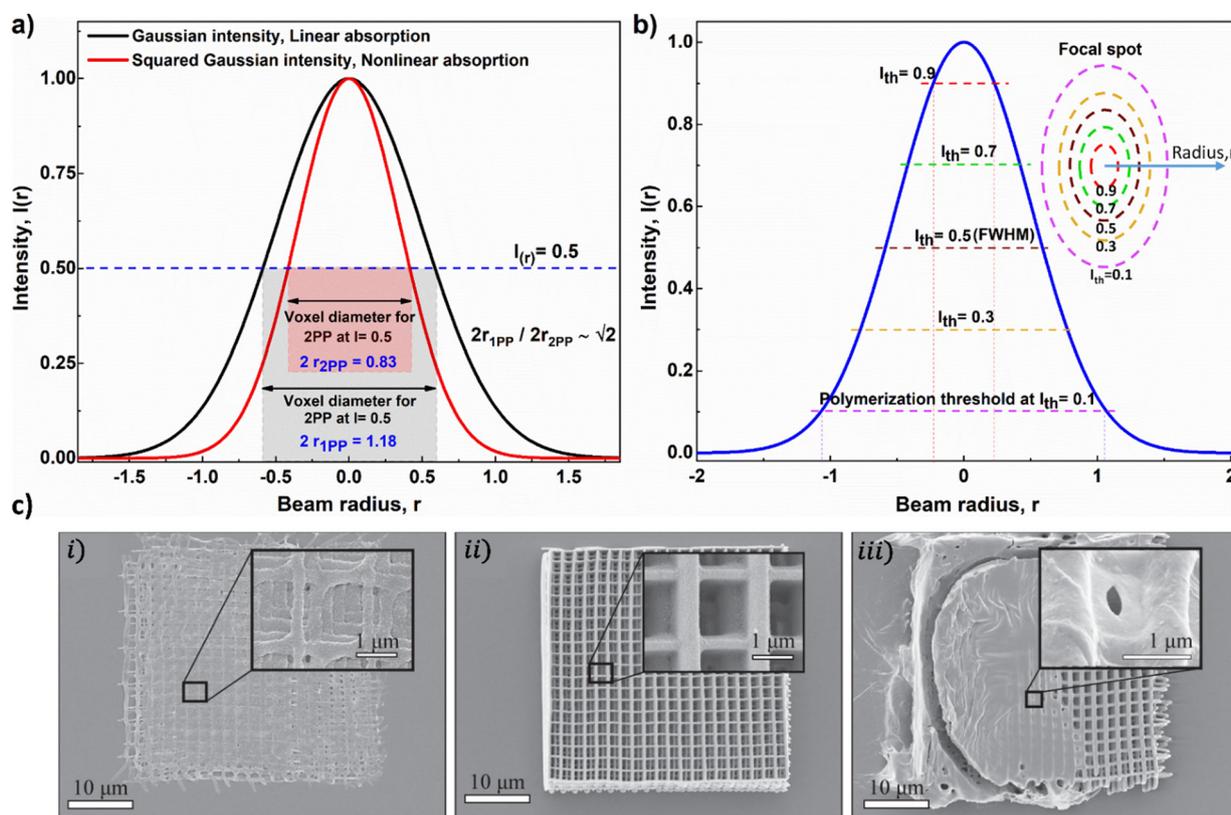

Fig. 11 (a) Light intensity distribution at the focal point of a Gaussian beam. The SLI distribution (red), relevant to the 2PA process, is reduced by a factor of $\sqrt{2}$ compared to the linear light intensity distribution (black), relevant to the 1PA process. This reduction is due to the NLO effect associated with 2PA. (b) Gaussian LFS size as a function of the intensity polymerization threshold. The focal size eligible for polymerization corresponds to the Gaussian beam size at the specified intensity threshold. The inset diagram compares LFS sizes associated with the Gaussian profile for different intensity thresholds. The size of LFSs in the scheme is in the same aspect ratio as the focal sizes in the Gaussian profile. The Gaussian beam profiles in (a) and (b) are provided for illustrative purposes. They were obtained using eqn (7), where $z = 0$ ($w_z = w_0$) and I_0, w_0 are taken as units. (c) Effect of exposure dose on the quality and stability of the 2PP-printed photonics microstructures. SEM micrographs of 3D woodpile photonic crystals fabricated at different exposure doses: (i) below the 2PP threshold, (ii) at the 2PP threshold, and (iii) above the 2PP threshold. (c) Reproduced under the terms of Creative Commons License CC BY 4.0.[146] Copyright 2015, the Authors, Published by MDPI.

18610 | *J. Mater. Chem. C*, 2025, **13**, 18597–18630

This journal is © The Royal Society of Chemistry 2025

resolution. Typically, the 2PP threshold is defined as the minimum peak intensity required to generate a sufficient concentration of radicals to initiate polymerization, ensuring the formation of stable solid polymer structures. By operating with an intensity slightly above the threshold level, only the central portion of the Gaussian beam, where the intensity exceeds the threshold, will solidify the liquid resin. The intensities that are below the threshold (*i.e.*, the edges of the Gaussian beam) will not affect the liquid state of the resin, and then no polymerization will occur (Fig. 11b).[12] For example, in a Gaussian beam with a standard peak intensity (I_0 =1), if the threshold intensity is set at $0.9I_0$, the resulting voxel size will be approximately 5 times smaller than when the threshold intensity is set at $0.1I_0$ (Fig. 11b). The size of these threshold-controlled features was found to be significantly influenced by the amount of oxygen dissolved in the resin. In fact, oxygen molecules act as quenching agents, inhibiting polymerization from propagating beyond the LFS center. At the center of the LFS, where intensity is high, the generated radicals can overcome the quenching effect of oxygen and initiate the 2PP reaction. However, at the edges of the LFS center, the intensity drops to a point where the rate of generated radicals can no longer overcome the oxygen quenching rate – that is the polymerization threshold.[143] This selective polymerization allows for the creation of features far beyond the diffraction limit of light. Therefore, precise control of the laser power or laser dose (power (P) × exposure time (Δt_{exp})) applied during 2PP processing is crucial to achieving such high-resolution features of microstructures.[18,73,144]

To theoretically determine the relationship between the voxel's dimensions, *i.e.*, lateral and longitudinal size, and laser intensity, approximated analytical models based on the Gaussian profile of the light intensity were developed.[25,145] The spatial intensity distribution of a focused Gaussian beam can be expressed as follows:

$$I_{(r,z)} = I_0 \frac{w_0^2}{w_{(z)}^2} e^{-2\left(\frac{r}{w_{(z)}}\right)^2} \quad (7)$$

where $I_{(r,z)}$ is the photon flux intensity at the point (r, z), and r and z denote the lateral and longitudinal distances from the center of the LFS/voxel, respectively. I_0 is the flux intensity of the incident photons at the center of the focused beam ($r = 0$ and $r = 0$). w_z is the beam radius, and it is expressed as:

$$w_{(z)} = w_0 \sqrt{1 + \left(\frac{z}{z_R}\right)} \quad (8)$$

where z_R is the Rayleigh length $\left(z_R = \frac{\pi w_0^2}{\lambda}\right)$. The polymerized voxel diameter ($D(r) = 2r$ at $z = 0$) and length ($L(z) = 2z$ at $r = 0$) can be derived from eqn (7).[145] By setting $I_{(r,z)} = I_{th}$ in eqn (7), $D(r)$ and $L(z)$ can be written as follows:

$$D(r) = w_0 \sqrt{\ln\left(\frac{I_0}{I_{th}}\right)} \quad (9)$$

$$L(z) = 2z_R \sqrt{\left(\frac{I_0}{I_{th}}\right)^{\frac{1}{2}} - 1} \quad (10)$$

I_{th} denotes the polymerization threshold intensity. Eqn (9) and (10) analytically demonstrate and confirm that the voxel's dimensions can be effectively controlled by adjusting the irradiation intensity $I_{(0)}$ with respect to I_{th}.

To achieve well-formed and stable polymerized structures, it is crucial to maintain the laser intensity within a specific processing window. While exceeding the polymerization threshold is necessary to initiate polymerization, excessive irradiation intensity can lead to structural distortion or damage. Therefore, precise control of laser intensity within the threshold window is essential to ensure efficient 2PP printing of stable, high-quality microstructures with finer features. Rybin *et al.*[146] investigated the impact of the exposure dose on the 2PP precision by fabricating 3D woodpile photonic crystals at different exposure levels: below, at, and above threshold levels (Fig. 11c). Their findings revealed that high exposure can distort and damage the finer features of the overall structure, as evidenced by the distorted and adhered crystal pillars in Fig. 11ciii. Conversely, insufficient exposure dose (below the threshold) can result in the loss of most of the unstable polymer structures during the washing step, which is caused by the insufficient polymerization (Fig. 11cii). Only maintaining the exposure dose within the appropriate processing window can result in freestanding and high-quality fabricated woodpile photonic crystal (Fig. 11cii).

The voxel's feature sizes are controlled by a multitude of factors beyond those considered in eqn (9) and (10). These factors encompass both the chemical properties of the resin, the experimental processing parameters, and the optical characteristics of the laser. Most of these parameter factors are already included in the term I_{th}. If the threshold condition is based on the radical density generation, the lateral size of the voxel, $D(r,t)$, can then be expressed as follows:[25]

$$D(r, t) = w_0 \sqrt{\ln\left(\frac{\sigma_a \Phi I_0^2 f \tau}{C} \Delta t_{exp}\right)} \quad (11)$$

where σ_a, f, Φ and τ are the 2PA initiator cross-section, radical's quantum yield generation, laser repetition rate, and pulse duration, respectively, Δt_{exp} is the exposure time, and C is defined as:

$$C = \ln[\rho_0(\rho_0 - \rho_{th})] \quad (12)$$

In eqn (12), ρ_0 represents the primary PI density and ρ_{th} denotes the radical density threshold, *i.e.*, the minimum concentration of radicals required to initiate the 2PP photoreaction and maintain stable microstructures. The relationship in eqn (11) provides a framework for controlling the voxel lateral dimension by adjusting various optical, material, and experimental parameters. For example, Haske *et al.*[18] empirically investigated the impact of average power (P_{avg}) and Δt_{exp} on the voxel lateral size. As predicted by eqn (11), they found that reducing both the P_{avg} and Δt_{exp} led to a significant decrease in voxel diameter. Furthermore, the use of PIs with high 2PA cross-sections was

This journal is © The Royal Society of Chemistry 2025

J. Mater. Chem. C, 2025, **13**, 18597–18630 | **18611**

found to considerably minimize the threshold P_{avg} and Δt_{exp}, which led to a substantial enhancement in 2PP resolution.[147] However, eqn (11) does not take into account other factors that affect voxel size. As a result, more comprehensive models have been developed, incorporating additional parameters, such as the order of multiphoton absorption (MPA), monomer concentration, and polymerization/termination rate constants. These advanced models provide greater flexibility in predicting and controlling the spatial resolution of the printed features (see, *e.g.*, Appendix B of ref. 148).

5.3. Other factors influencing 2PP resolution

Advances and optimizations in the optical system have also significantly enhanced 2PP resolution. For example, controlling the exposure dose using a mechanical shutter (pinpoint scanning mode (PSM)) often results in lower resolution features due to the longer exposure times associated with the slower mechanical responses of the shutter. Alternatively, continuous scan mode (CSM) offers a more effective approach to achieving higher 2PP resolution by adjusting the laser power and scan speed.[149,150] Tan *et al.*[149] demonstrated that optimizing the printing speed to 600 μm s^{-1} achieves an impressive linewidth of 23 nm, highlighting the advantage of precise speed control in enhancing feature resolution. However, despite the high resolution achieved with this approach, it is not suitable for many applications requiring specialized microstructure geometries. The insertion of a frequency-doubling crystal (*e.g.*, β-BaB$_2$O$_4$ (BBO)) into the Fs-laser printing setup is a new effective approach used to shift Fs laser wavelength from the IR to visible region, allowing the reduction of the excitation wavelength by half ($\lambda/2$) and triggering polymerization in the deep UV (DUV) region.[151,152] This approach helps overcome the light diffraction limit associated with λ and, thus, enhances the 2PP feature resolution. In fact, as seen in eqn (9) and (10), the length and diameter of the voxel are proportional to w_0, which is, in turn, is directly proportional to λ (eqn (6)). Therefore, reducing λ will strongly reduce the voxel dimension and improve the spatial resolution. Fig. 12a illustrates an energy diagram for Vis 2PA that enables polymerization in the DUV region. A schematic of the optical setup used for converting Fs-pulsed IR excitation ($\lambda = 800$ nm) to Vis Fs pulses ($\lambda = 400$ nm) is shown in Fig. 12a. Taguchi *et al.*[30] used the DUV-assisted 2PP printing approach to print microstructures of 80 nm feature size, *i.e.*, $\lambda/5$ resolution (Fig. 12c). Additionally, they successfully fabricated stacked fine microstructures comprising a series of trenches as narrow as 35 nm (Fig. 12d). Interestingly, they found that the intensity required to trigger DUV-2PP was 7 times lower than that needed for conventional IR Fs-assisted 2PP under the same
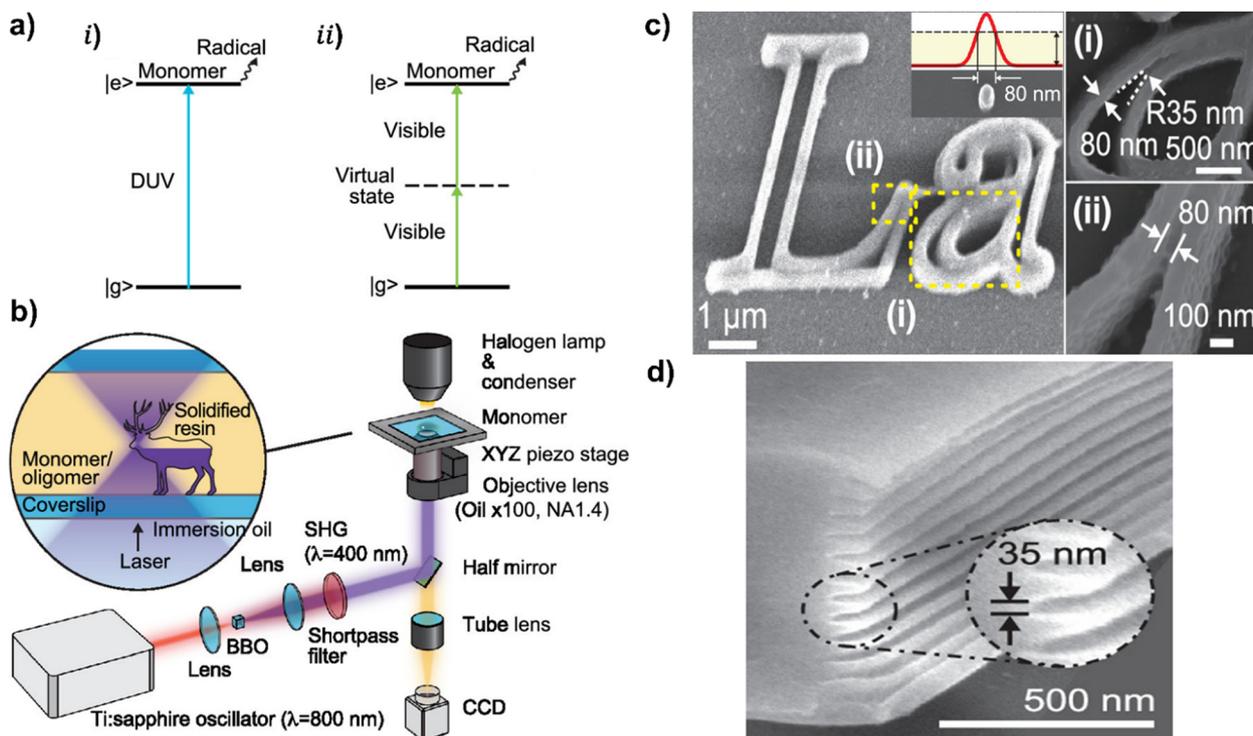

Fig. 12 Application of 2PE using a pulsed visible wavelength ($\lambda = 400$ nm) to achieve energetically equivalent DUV excitation ($\lambda = 200$ nm) for 2PP printing. (a) Energy diagram of polymerization in DUV using (i) one-photon DUV excitation, and (ii) two-photon Fs-visible excitation. (b) Optical setup for DUV lithography. A BBO crystal was used to convert the IR Fs laser wavelength ($\lambda = 800$ nm) to visible wavelength ($\lambda = 400$ nm). Two photons of $\lambda = 400$ nm are equivalent to one photon of $\lambda = 200$ nm, corresponding to DUV excitation. (c) SEM micrograph of 'La' letters printed by DUV-2PP. The marked regions (i) and (ii) in (c) (left) are enlarged in the right-hand panels, showing the features resolution. The inset shows the smallest printed voxel of 80 nm width. (d) SEM micrograph of fine structures comprising a set of deep trenches, each 35 nm wide. (a)–(d) Reproduced with permission.[30] Copyright 2020, American Chemical Society (ACS).

18612 | *J. Mater. Chem. C*, 2025, **13**, 18597–18630

This journal is © The Royal Society of Chemistry 2025

conditions. Moreover, they were able to fabricate all these microstructures without the use of PIs or photosensitizers, as the two-photon energy (corresponding to 200 nm) directly overlaps with the absorption band of the photopolymerizable monomers in the DUV region. This unique feature of PI-free 2PP has recently gained significant attention in the biomedical field, where PI toxicity presents a major concern.[31,152]

Optical photoinhibition techniques, such as stimulated emission depletion (STED) and resolution augmentation through photo-induced deactivation (RAPID), have been instrumental in eliminating the Abbe's diffraction barrier and thereby remarkably improving 2PP resolution.[21,140] In conventional 2PP, PI molecules in the ground singlet state S_0 are promoted to the excited singlet state S1 by 2PA, then undergo intersystem crossing to triplet state (T_1) and generate radicals that initiate polymerization. The original idea of the STED inhibition approach is to prevent polymerization by inducing stimulated emission from S_1 back to S_0 before intersystem crossing takes place. This is achieved by exposing the PIs to light with a wavelength (typically in the visible range) matching the $S_1 \rightarrow S_0$ energy gap, leading to effective depopulation of the S_1 state.[61,153,154] On the other hand, the RAPID approach employs a distinct inhibition pathway, which involves depleting the triplet state (T_1) through non-radiative relaxation, typically using a wavelength similar to the excitation (writing) beam ($\sim$800 nm).[60,140]

Researchers have exploited these photoinhibition approaches and designed innovative phase-shaped focused beams, such as donut focus and bottle-beam focus, to minimize voxel size and, therefore, improve 2PP resolution.[100,140] For example, the doughnut-shaped beam profile shown in Fig. 13d exhibits zero intensity at the focal center and non-zero inhibition intensity at the transversal edges. Accordingly, this donut-shaped configuration can effectively reduce the voxel lateral size by photoinhibiting polymerization in the x–y directions of the voxel. Gan et al.[63] reported the effectiveness of this doughnut-shaped inhibition approach in 2PL by achieving deep sub-diffraction feature sizes below 10 nm; comparable to those obtained with EBL and EUV. First, they reduced the width of the printed nanowire from 152 nm to 42 nm through laser power adjustment (threshold effect) (Fig. 13a). Then, by using the donut-shaped inhibition beam, they further reduced the feature size from 42 nm to 9 nm by increasing the inhibition beam intensity (Fig. 13b and c).
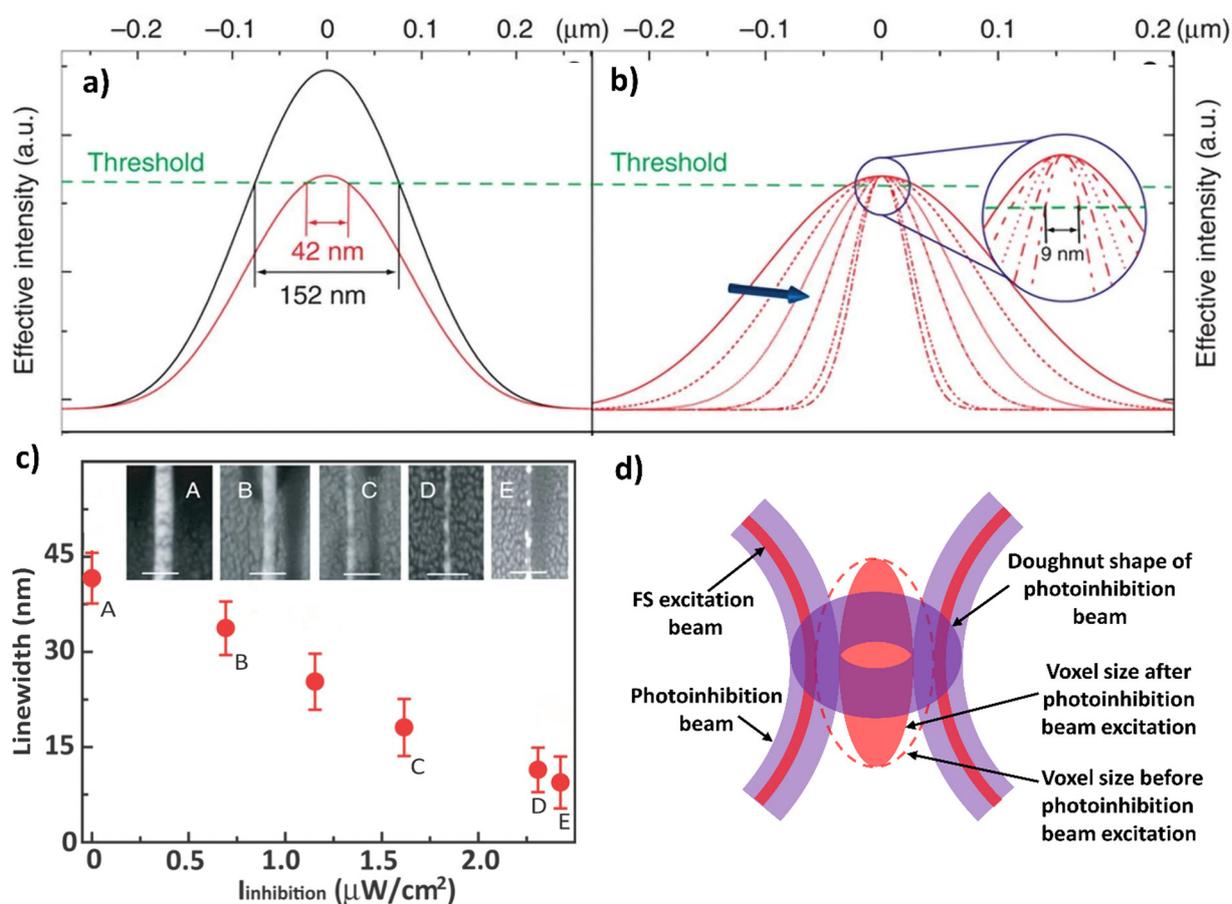

Fig. 13 Schematic demonstration illustrating feature size reduction by (a) the polymerization threshold effect (linewidth reduction from 152 to 42 nm), and by (b) increasing photoinhibition beam intensity (linewidth reduction from 42 nm to 9 nm). (c) Effect of increasing photoinhibition intensity on the linewidth of printed nanowires (scale bar: 100 nm). (a)–(c) Reproduced under the terms of the Creative Commons License CC BY 4.0.[63] Copyright 2013, the Authors, Springer Nature. (c) Reproduced with modifications. (d) Schematic illustration of the doughnut-shaped beam inhibition mechanism. Redrawn based on ref. 100, Springer Nature.

This journal is © The Royal Society of Chemistry 2025

J. Mater. Chem. C, 2025, 13, 18597–18630 | 18613

STED and RAPID lithography have demonstrated significant advantages over standard 2PP, typically enhancing resolution nearly 2-fold by halving the voxel size to around 40–60 nm.[21,155,156] However, this enhancement comes with notable trade-offs. Both techniques, especially STED, require highly sophisticated optical configurations, involving precise spatio-temporal synchronization between excitation and depletion beams within the focal volume. This added complexity can nearly double the cost of a standard 2PP system while reducing printing speed. Furthermore, these approaches are not compatible with all photoresists, as they typically demand specially engineered PIs and higher-powered lasers, thereby restricting the choice of resins and increasing energy requirements.[61,140,157] Unlike optical inhibition, chemical inhibition through incorporating radical inhibitors into the resin mixture offers a highly effective and economical alternative. Much like the action of oxygen quenchers previously discussed, these inhibitor molecules help to control the reaction process by lowering the 2PP threshold and limiting radical diffusion, resulting in a dramatic reduction in voxel size and a consequent resolution improvement.[158,159] Using this approach, Farasi's group[160] successfully fabricated complex 3D structures with feature sizes as small as 60 nm.

5.4. Surface smoothness accuracy in 2PL

Alongside the feature resolution, the surface smoothness of fabricated microstructures is another critical aspect that researchers are constantly trying to improve. This is particularly important for microstructures requiring high-precision surfaces, such as optical microlenses and photonics microdevices.[21,161,162]

In addition to the size of individual polymerized voxels, the spatial arrangement of voxels within the microstructures also plays a crucial role in the accuracy and quality of 3D microstructures. The 3D stacking of voxels is characterized by their size, defined by diameter (d) and length (l), and the distance between them in the x and z directions (dx and dz, respectively). The voxel overlap parameter (δ) is given by the following equation:[47]

$$\delta = \frac{d - dx}{d} \times \frac{l - lz}{l} \tag{13}$$

Zhou et al.[21] numerically established the relationship between the surface roughness of the printed structures, voxel size, and voxel overlap. Their numerical findings demonstrated that higher voxel overlap with finer voxel sizes are key factors in achieving smooth surfaces. Takada et al.[159] confirmed this demonstration empirically and found that reducing the distance between adjacent voxels (high voxel's overlapping) reduces surface roughness significantly, and thereby improves the smoothness/surface quality of microstructures (Fig. 14a). Sun's group[162] further demonstrated the effectiveness of small-sized voxels and their spatial overlap in the fabrication of high-precision aspheric microlens, achieving an estimated surface roughness of just 2.5 nm (Fig. 14bi). The parabolic profile of the aspheric printed microlens was found to match very well with the theoretical parabolic curve (0.2% error) (Fig. 14bii), which is considered far better than any other high-precision fabrication techniques.[162] In fact, when voxel overlap is sufficiently high, the surface roughness becomes negligible due to the Gibbs free energy that favors self-polymerization and self-smoothing effects at the concave edges of the voxel ends (Fig. 14c).[5,161]
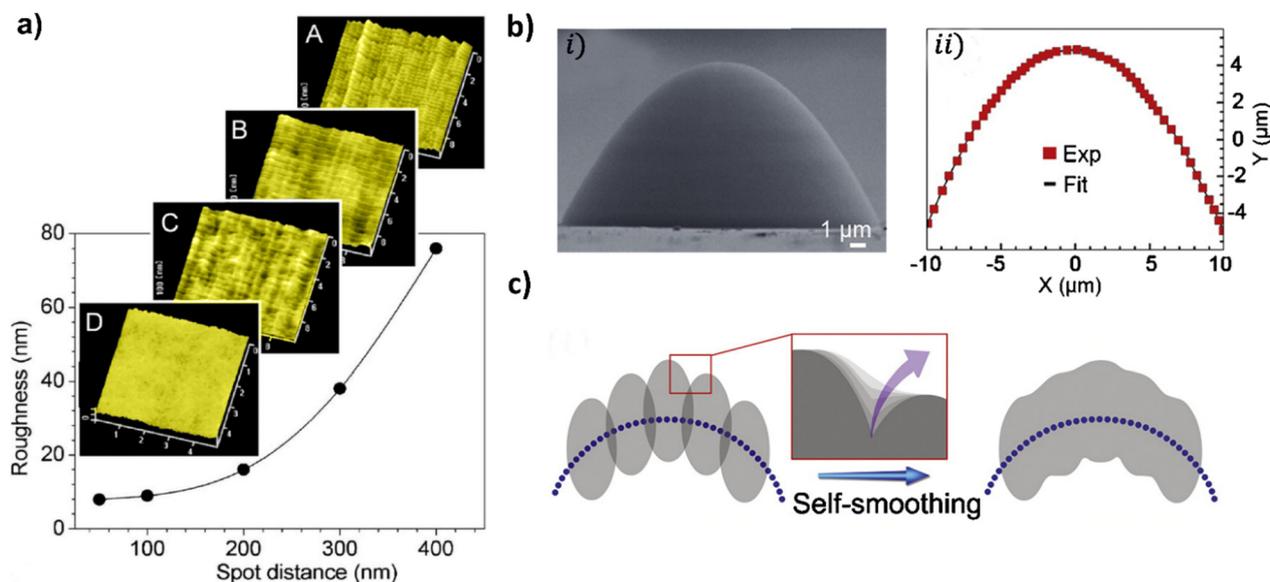

Fig. 14 Effect of voxel's overlap on the surface quality of the laser-printed microstructures. (a) Relationship between the roughness and voxel overlap (voxel distance). The AFM images illustrate the evolution of surface roughness as the voxel distance decreases from 300 nm (micrograph A) to 100 nm (B) and finally to 50 nm (C). Micrograph D is a spin-coated polymer surface that was taken as a reference. Reproduced (with modifications) with permission.[159] Copyright 2005, AIP Publishing. (b) (i) Side view SEM micrograph of 2PP-printed aspheric parabolic microlens. (ii) Measured profile of the microlens shown in (b) (i) (red square) and the corresponding theoretical fit (solid black line). (c) An illustrative model showing how surface quality is enhanced (reduced roughness) through the self-smoothing effect occurring at the concave edges of the overlapped voxels. (b) and (c) Reproduced with permission.[5] Copyright 2010, Elsevier. (b) Originally published in ref. 162, Copyright © 2009, IEEE.

18614 | J. Mater. Chem. C, 2025, 13, 18597–18630

This journal is © The Royal Society of Chemistry 2025

5.5. Optimizing resolution and throughput

While the aforementioned techniques enable achieving small feature sizes, these dimensions must be evaluated within the context of the entire manufacturing framework. In fact, the high 2PP-resolution can become a bottleneck, as it inherently restricts printing throughput (increases printing time), which is a key parameter for industrial-scale manufacturing. A generalized empirical law for 3D lithography – adapted from Tennant's law originally formulated for 2D lithography[163] – provides a relationship between the printing throughput, T_{3D} (μm^3 h^{-1}) and the feature resolution, Res (nm) as follows:[164]

$$\text{Res} = C \times T_{3D}^{0.3} \text{ or } T_{3D} = C' \times (\text{Res})^3 \qquad (14)$$

where C ($C' = 1/C^3$) is a constant that depends on the efficiency of the process. The third power scaling in eqn (14) illustrates that improving spatial resolution (*i.e.*, finer features) drastically reduces the processing throughput, while shortening fabrication time (*i.e.*, increasing throughput) comes at a severe resolution penalty. In practical applications, optimizing one parameter often compromises another, making it necessary to achieve an optimal trade-off. Most commercially available 2PL systems are configured to offer resolutions in the range of $\sim$100 nm to over 1 μm, as a trade-off to maintain reasonable printing speeds.[112,165,166] In recent years, manufacturers have begun offering application-specific 2PL systems tailored for specialized tasks; applications that demand ultra-high precision, such as micro-optics, require 2PL systems equipped with high NA OL and operate at lower laser powers,[167] while large-scale or high-throughput applications that are less sensitive to resolution can be efficiently fabricated using systems that employ low-NA OL combined with higher irradiation laser powers (*e.g.*, NanoOne$_{1000}$, UpNano).[166,168]

In light-based 3D printing, throughput is usually defined as the rate at which a volume is fabricated and is typically measured in mm^3 s^{-1} or μm^3 s^{-1}. However, this volumetric measure does not adequately reflect the impact of resolution, which is a critical factor influencing manufacturing time. For instance, producing a high-resolution structure with finer features can require considerably more time than fabricating the same structure volume composed of larger voxels (*i.e.*, low resolution). As a result, modern formulations now express throughput in voxels per second (voxel per s), which effectively accounts for variations in resolution and provides a more meaningful comparison across different 3D printing systems.[81,169]

In recent years, considerable efforts have been made to improve the 2PL throughput, making it among the fastest 3D printing techniques while maintaining respectable resolution. Fig. 15 provides a quantitative comparison of voxel size and throughput (in voxel per s) for various 3D printing technologies, highlighting the significant advancements in 2PL's printing speed, which now surpass many conventional additive manufacturing methods. Nevertheless, despite these improvements, current 2PP printing speeds remain significantly lower, especially when compared to interference lithography and nanoimprint lithography[170] (though they are not considered true 3D printing techniques), which still limits 2PL's competitiveness

for industrial-scale applications. Additionally, the high cost of 2PL setup – especially when combined with advanced systems like STED or expensive scanners – poses a major barrier to widespread adoption. In response, recent developments have extensively focused on system miniaturization, cost reduction, and enhanced throughput (see Section 7). These innovations have promise for establishing 2PL as a viable and leading technology for industrial-scale 3D manufacturing.

6. Applications of 2PP-assisted 3D nanoprinting

This section explores various applications of 2PP-assisted 3D laser lithography that significantly contribute to the advancement of scientific and technological fields. Here, we highlight the transformative impact of 2PL in three key areas: micro-optics, where 2PL revolutionizes the field by enabling the design of miniaturized and complex optical systems suited for a wide range of applications; microelectronics and micro-optoelectronics, where 2PL enables the development of advanced opto-/electronics multifunctional devices in high demand for a variety of applications; and biomedical engineering, which leverages 2PL for innovative soft microrobots and diagnostics, *i.e.*, functional micromachines. These applications highlight the significant role of 2PL in shaping future technologies.

6.1. Micro-optical components

Although still relatively new compared to other lithography techniques, no other competing technology matches 2PL in terms of performance and simplicity for fabricating micro-optical components.[46,171] Indeed, 2PL offers promising solutions to many challenges facing micro-optical component manufacturing, enabling high precision, rapid prototyping, and high quality in the fabrication of miniaturized and complex optical systems.[46,172–174] Gissibl *et al.*[43] demonstrated the fabrication of a complex aspheric triplet lens system that compensates for chromatic aberrations and improves imaging quality (Fig. 16ai). They also showcased the feasibility of 2PL for microscale endoscopic applications by fabricating an array of these triplet lenses on the end facet of a 210 μm-diameter fiber, which exhibits outstanding imaging performance (Fig. 16aii). In another work, the same group[175] fabricated complex micro-optics by 3D printing a range of aligned optical elements with specific functionalities directly onto the top face of single-mode fibers (SMFs). The fabricated optical fibers revealed excellent performance for beam collimation, astigmatism correction, intensity shaping, and polarization control simultaneously. Furthermore, 2PL has shown great capabilities for the fabrication of complex, highly miniaturized, high-quality multi-component imaging cameras that mimic the natural vision of predators (*e.g.*, eagle eye), where the resolution of vision increases towards the center of the field of view, *i.e.*, foveated vision. Thiele *et al.*[176] demonstrated the 3D printing of a set of multi-lens objective systems onto a complementary metal-oxide-semiconductor (CMOS) sensor, each system combining four printed doublet lenses with different focal
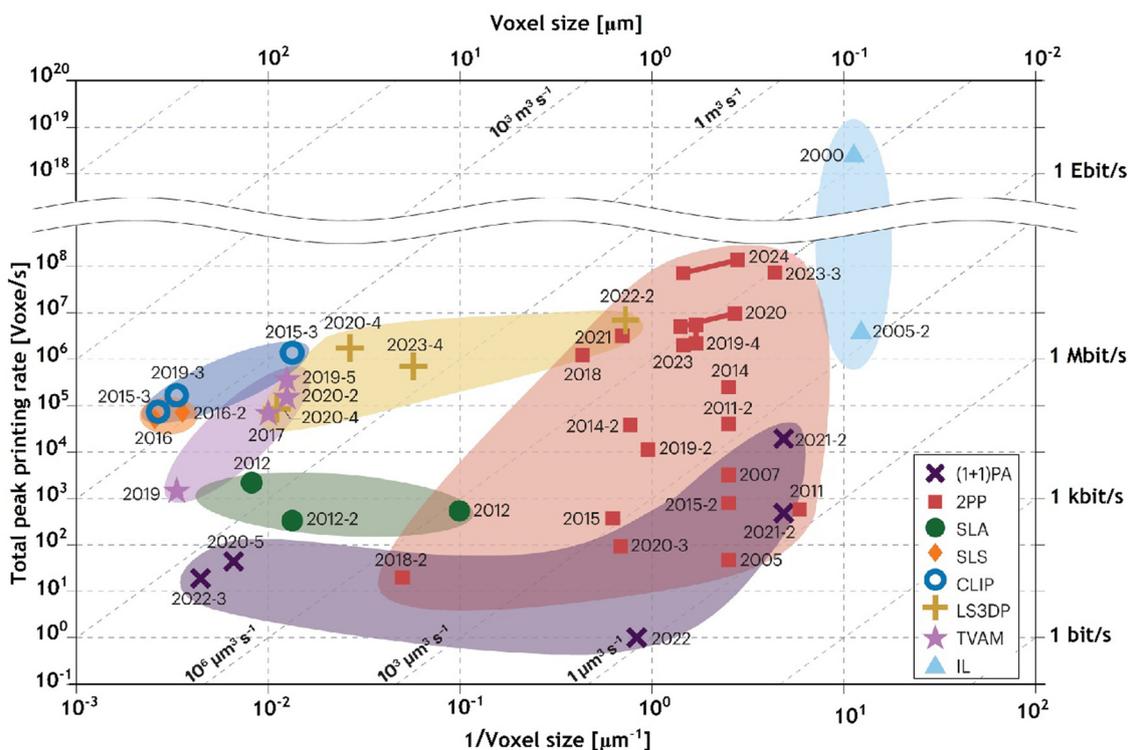
Fig. 15   Comparison of various 3D printing techniques based on their maximum printing speed (throughput) and achievable voxel resolution. The reported voxel size reported represents the average of its lateral and longitude axial (longitudinal) dimensions. SLA: stereolithography; CLIP: continuous liquid interface printing; SLS: selective laser sintering; (1 + 1) PA: (1 + 1)-photon absorption; LS3DP: light-sheet 3D printing; TVAM: tomographic volumetric additive manufacturing; IL: interference lithography; 2PP: two-photon polymerization (two-photon 3-D laser printing). Adapted with permission from ref. 156, Copyright © 2023, Springer Nature Limited. Originally published in ref. 81, CC BY 4.0. A more detailed and regularly updated version of this figure is available at https://3dprintingspeed.com.

lengths (*i.e.*, different fields of view) (Fig. 16bi), enabling a wide viewing angle of 70° with a significant increase in angular resolution at the center of the image (Fig. 16aii). The fabricated micro-scale foveated camera can be used in microdrones, comparable in size to an insect, to simultaneously capture a wide-angle view and detailed images of specific areas.

2PL has also shown great potential for manufacturing sub-micrometer optics for X-ray manipulation over a wide energy range. Sanli *et al.*[177] fabricated an achromatic X-ray optic composed of a 2PP-printed defocusing refractive lens combining four parabolic μ-lenses and an EBL-printed focusing diffractive lens (Fig. 16ci). The printed achromatic system showed superior correction of chromatic aberration over a wide range of X-ray energies compared with the use of a single focusing diffractive lens (Fig. 16ciii). The same team[178] also reported the 3D fabrication of a high-performance apochromatic X-ray lens system comprising six specific defocusing lenses printed using 2PL. The printed apochromatic X-ray system improved the range of chromatic aberration correction by four times compared with the achromatic system, demonstrating the great ability of 2PL for printing systems that efficiently manipulate X-rays over a wide wavelength range, and thus enabling the prospective use of X-rays in microscopy and imaging applications. Recently, 2PL has shown great potential for manufacturing metalens systems that are more sophisticated than conventional

refractive/diffractive lenses due to their ultra-compact, multi-functional, and ultra-thin characteristics, as well as their higher degree of light manipulation.[46,172] Ren *et al.*[179] designed a 3D achromatic metalens on the top surface of an SMF (*i.e.*, meta-fibers) (Fig. 16di), which enabled efficient light focusing over the entire NIR telecommunication band (1.25–1.65 μm) without color distortion and independently of polarization. They also reported the potential of the 2PP-printed achromatic meta-fibers for confocal fiber-optic imaging, producing brighter and clearer images than their chromatic counterparts over a wide range of wavelengths (Fig. 16dii). Meanwhile, Balli *et al.*[180] designed a hybrid 3D achromatic metalens, which combines a phase plate and a nanohole-structured metalens, capable of achieving excellent focusing efficiency and achromatic imaging on ultra-broadband light illumination spanning from Vis light to short-wave IR (450–1700 nm). Furthermore, 2PL has demonstrated its exceptional ability to 3D print promising micro-optical elements for spectroscopy and microscopy. Bogucki *et al.*[181] developed a 3D elliptical microlens system (Fig. 16ei) that efficiently collects light from nano-sized light emitters and reshapes its divergence, which enables a more than 70-fold increase in the working distance (Fig. 16eii). The 2PP printed aspheric μ-lens arrays were used for spectroscopic measurements on a variety of materials (*e.g.*, quantum dots), demonstrating significantly improved signal collection efficiency while
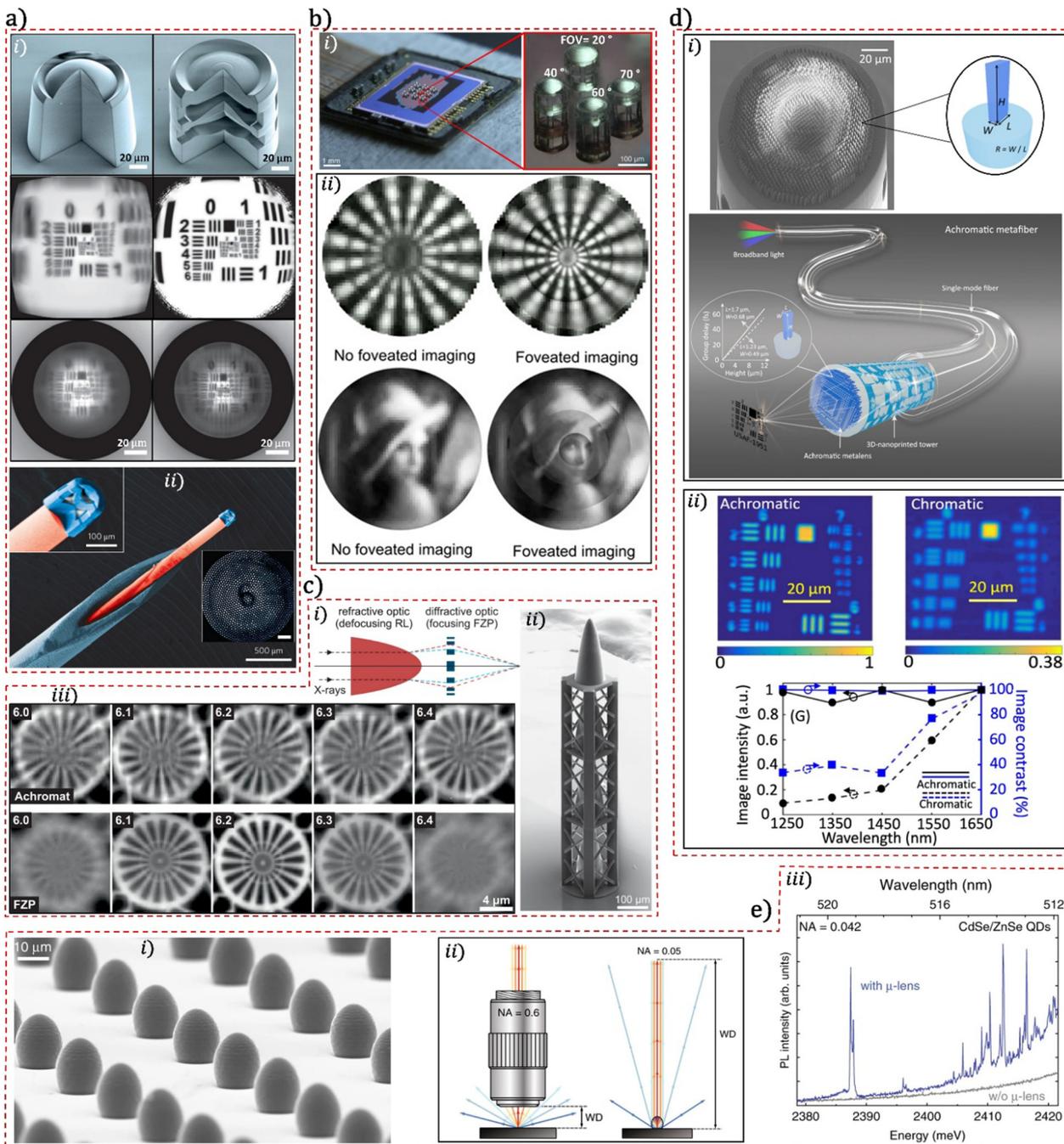
utilizing extremely low NA optics over a wide range of spectral bands (Fig. 16eiii). Thanks to 2PL, this finding effectively addresses the experimental limitations imposed by bulky high-NA microscope objectives and opens the way to a wide range of modern optical measurements.

Since all the applications highlighted above are very recent, and research in this field is still in its infancy, the major potential of 2PL in micro/nano-optics has yet to be fully exploited. Therefore, with the continued development and improvement of photoprintable materials and the 2PL system, there will be exciting new opportunities to develop micro-optical systems that were previously unthinkable, opening up new prospects for more advanced applications.

6.2. Microelectronic and micro-optoelectronic devices

The ever-increasing use of technology has rapidly increased the need to manufacture miniaturized, high-precision, and multi-functional 3D electronic microdevices, such as micro-energy storage devices, bioelectronics, and photodetection microdevices. While conventional planar lithography techniques fall short of meeting all these advanced requirements, 2PL offers the promise of a true 3D manufacturing technique for the fabrication of high-precision and high-performance conductive electronic microstructures.[121,182,183] However, the limitation of precursor conductive photoresists poses a critical challenge for printing highly functional microelectronic devices. This problem is being successfully addressed by integrating conductive materials, such as CNTs and conductive polymers, into the photoresists.[182,184,185] A major challenge of this approach is incorporating the maximum amount of conductive materials into the resists without forming clumps and aggregates that dampen the NL absorption and thus limit polymerization.[186] W. Xiong et al.[64] utilized a CNT-embedded polymer photoresist to fabricate conductive 3D microarchitectures using 2PL. They used the thiol grafting method to functionalize multiwall carbon nanotubes (MWNTs) and anchor them to the polymer resin. This enabled them to develop MWNT-thiol-acrylate (MTA) composite resins with high MWNT grafting concentrations, while maintaining excellent stability, miscibility, and high MWNT dispersion in the composite resin. To investigate the anisotropy effect on the electrical conductivity of the printed microdevices, they fabricated two bar-shaped channels for connecting two pairs of gold (Au) electrodes, using two 2PP-scanning directions: one parallel and the other perpendicular to the long bar axis (Fig. 17ai). Interestingly, their investigation revealed that MWNTs are strongly oriented in the direction of laser scanning, thus selectively improving the electrical conductivity of the microstructures (Fig. 17aii). This MWNTs orientation feature is very important in many electronics and optoelectronics applications, as it allows rising electrical and optical anisotropic properties inside the functional microdevices.[187,188] To showcase the potential of MWNT-based resin in microelectronic applications, the same team[64] used 2PP to fabricate two complex electronic arrays of micro-capacitors (Fig. 17aiii) and micro-resistors (Fig. 17av). The printed micro-capacitor array, consisting of ten capacitors connected in parallel, exhibited a typical hysteresis loop with a high

capacitance value of 50 pF, demonstrating relatively high storage performance (Fig. 17aiv). The AC impedance of the printed micro-resistor array exhibited stable and high resisting performance at low-frequency range, which then dropped with increasing frequency, demonstrating exceptionally high electrical conductance at higher frequencies (Fig. 17avi). This high high-frequency electrical conductance of printed CNT-based microdevices is promising for many high frequency electronic applications, such as radio-frequency (RF) electronics.[189,190]

D-Toussi et al.[191] reported the integration of organic semiconductor (OS) polymers for manufacturing highly conductive functional microelectronics devices. They embedded the OS of PEDOT:PSS (poly(3,4 ethylene-dioxy-thiophene):poly(styrene-sulfonate)) into the photoresist matrix to fabricate a functional micro-printed circuit board (μ-PCB) that integrates various electrical elements (Fig. 17bi). The fabricated μ-PCB exhibited different resistor/conductor behaviors of the various electrical elements printed on it (Fig. 17bii). They also designed highly functional microelectronic biosensors (Fig. 17biii) by incorporating biorecognition molecules (i.e., glucose oxidase enzyme (GOx) for glucose sensing) into the OS composite material (OSCM). Amperometry response measurements conducted on the μ-printed GOx/OSCM-based biosensor showed a significant current response as a function of injected glucose concentrations, demonstrating the high functionality of the printed microelectronic biosensor (Fig. 17biv). This biosensor also demonstrated excellent sensitivity for glucose (232.9 ± 22.5 μA mm^{-1} cm^{-2}) (Fig. 17bv), which proved much higher than the majority of other GOx immobilization reported methods.[191]

Furthermore, the μ-printed biosensor revealed a response time of only ~4 s and a reproducibility/precision (relative standard deviation, RSD) of ~4.02%, which is much lower than that reported by the Food and Drug Administration (RSD; 15%).[191,192] Consequently, these results highlighted the high capability of 2PL to manufacture microelectronic biosensors with excellent functionality, which are in high demand for detection and sensing applications.

2PL also offers potential capabilities for fabricating highly functional semiconductor optoelectronic devices. Liu et al.[193] benefited from the high 2PL-structuring capabilities and high uniformity of the metal-bound composite photoresin (metal–organic framework (MOF)-based photoresin) to print a high-precision, high-performant 3D metal oxide microarchitecture of the ZnO UV μ-photodetector. A schematic illustration of the operating mechanism of the ZnO UV photodetector is shown in Fig. 17ci. Its operating principle is based on the photoelectric effect, where under UV illumination, electron–hole pairs are generated, leading to the desorption of oxygen and then the generation of an output current under an applied external bias.[194,195] The μ-printed ZnO UV photodetector exhibited excellent sensitivity for UV light detection, with a high ON/OFF ratio of about 3000 under an external bias of 20 V (Fig. 17cii).[193] Moreover, time-resolved photoresponse measurements showed multiple symmetrical ON/OFF cycles with a rise and decay photocurrent time of 31 s and 44 s respectively (Fig. 17ciii), demonstrating the fast photo-responsivity and the high cycling

18618 | J. Mater. Chem. C, 2025, **13**, 18597–18630

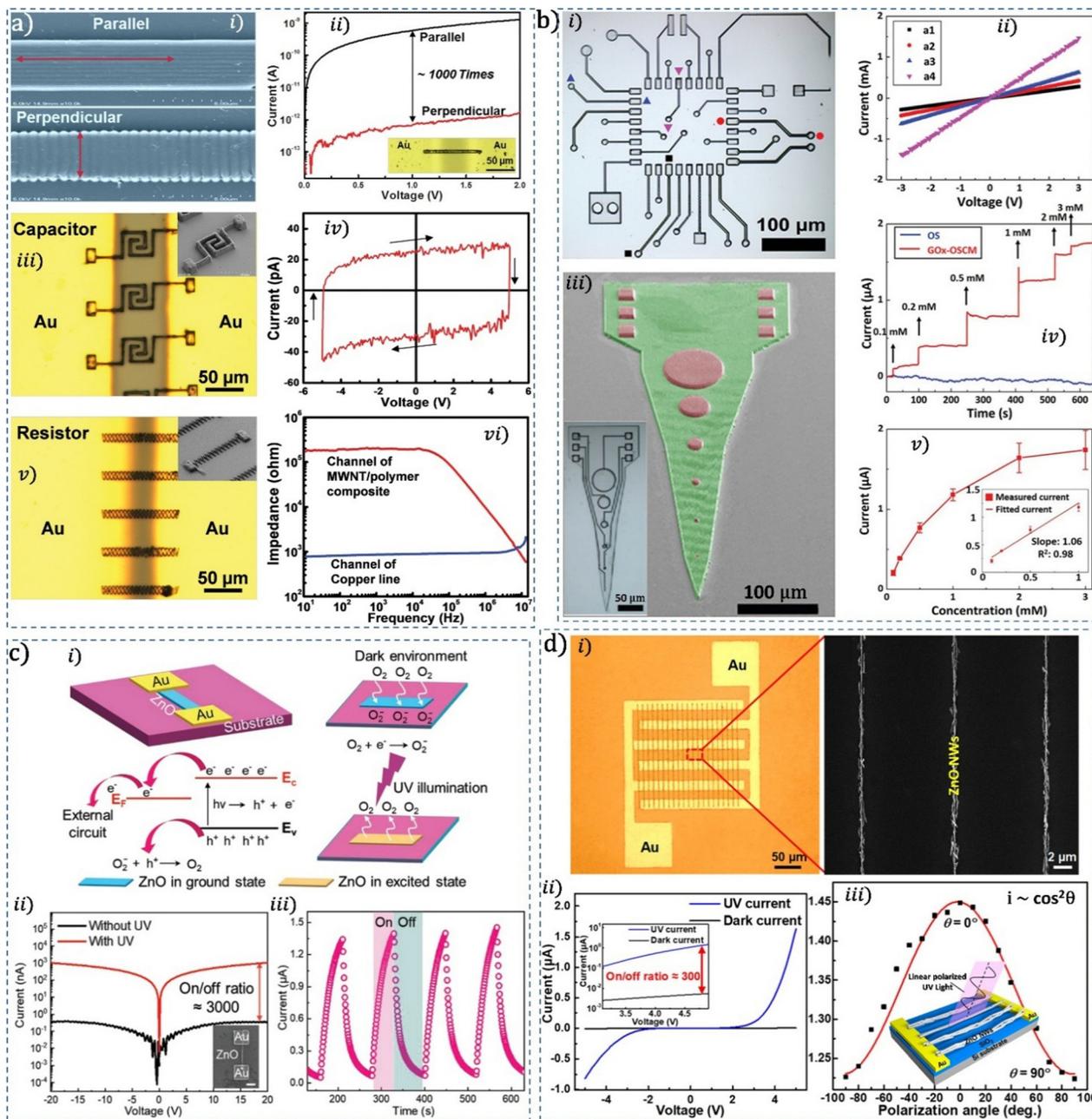This journal is © The Royal Society of Chemistry 2025

Fig. 17   2PL-based 3D printed microelectronic and micro-optoelectronic devices. (a) (i) SEM micrographs of two bar-shaped channels connecting two Au electrodes, printed using two laser scanning directions: (top) parallel and (bottom) perpendicular to the long bar axis. (ii) $I-V$ curves of the two-channel bars shown in (i); inset: optical micrograph of the channel bar connecting two Au electrodes. Optical and SEM (insets) micrographs of a μ-printed (iii) capacitor and (v) resistor arrays bridging two Au electrodes, and their corresponding (iv) capacitance and (vi) AC impedance characterizations, respectively. Reproduced with permission.[64] Copyright 2016, Wiley-VCH. (b) (i) Optical image of a μ-PCB integrating various electrical elements, and (ii) represents the $I-V$ curves of the electrical elements on the μ-PCB. (iii) Pseudo-colored SEM micrograph of a printed biosensor microelectrode (red represents the OS composite polymer and green represents the bare polymer); inset: optical image of the μ-biosensor. (iv) Amperometry response measurements as a function of successive injected glucose concentrations for the μ-printed OSCM- and GOx/OSCM-based biosensors. (v) Response curve (calibration curve) of the μ-printed GOx/OSCM biosensor. Reproduced with permission.[191] Copyright 2022, Wiley-VCH. (c) (i) Schematic illustration of the ZnO UV photodetector. (ii) $I-V$ curves of the printed ZnO UV μ-photodetector in the dark and under 365 nm UV illumination; inset: SEM image of the ZnO UV μ-photodetector. (iii) Photo-response time of the ZnO UV μ-photodetector under a 20 V bias voltage. Reproduced with permission.[193] Copyright 2021, Wiley-VCH. (d) (i) (left) optical and (right) SEM micrographs of the aligned ZnO NWs bridging the pre-deposited interdigital Au electrodes. (ii) The ON/OFF ratio of the ZnO NW-based polarized μ-photodetector with and without UV illumination. (iii) Photocurrent response of the UV μ-detector as a function of the polarization angle of the UV light. $\theta = 0°$ means the UV light polarization is parallel to the NW arrays, as shown in the inset, while $\theta = 90°$ means the polarization is perpendicular. The red solid line represents the theoretical fit to the experimental data (black dots), following a $\cos^2 \theta$ function (malus law). Reproduced with permission.[196] Copyright 2020, American Chemical Society (ACS).

This journal is © The Royal Society of Chemistry 2025

J. Mater. Chem. C, 2025, 13, 18597–18630 | 18619

stability of the printed ZnO μ-photodetector.[193] In parallel, Long et al.[196] successfully assembled ZnO NWs with precise orientation control and fabricated a polarization-resolved UV microdetector with excellent performance using 2PL. The optical and SEM micrographs of the printed aligned ZnO NWs on the pre-deposited interdigital Au electrodes are shown in Fig. 17di. The photodetector exhibited a high ON/OFF ratio of 300 and exceptional photoresponsivity (4×10^4 A W^{-1}), under 365 nm UV illumination and 4.75 V external bias (Fig. 17dii). They[196] also investigated the anisotropic characteristics of aligned ZnO NWs by measuring the photocurrent response of the μ-photodetector as a function of the polarization angle of UV light (Fig. 17diii), demonstrating the successful design and functionality of the polarized UV μ-detector printed using 2PL.

Consequently, through the design of conductive, anisotropic, and homogeneous 2PA materials, 2PP printing has demonstrated superior potential in fabricating arbitrary 2D/3D conductive microdevices that exhibit exceptional performance and are highly desirable for various electronic and optoelectronic applications. By pursuing the development of highly conductive, anisotropic, and photoconductive photoresist materials, 2PL promises to open up new prospects for manufacturing advanced 3D electronic and optoelectronic microdevices with high levels of miniaturization and superior functionality.

6.3. Soft microrobots for biomedical applications

Multi-functional and mobile microrobots, comparable to human blood cells (∼10 μm in size), are now achievable thanks to advances in 2PL.[197–203] Various types of these microscale printed robots have been evaluated both in vitro and in vivo, notably for their motion capabilities as micromachines capable of moving and performing complex tasks on the μm-scale.[204,205] Magnetic microswimmers (MSs), 3D printed using 2PP with user-defined geometries and magnetic responsiveness, have shown potential promise for a variety of biomedical applications, including targeted drug delivery,[62,206–209] sensing/diagnosis,[202,210] and microsurgery.[211–213] Fabricated from non-toxic and biodegradable materials such as hydrogel gelatin methacryloyl (GelMA), these helical micromachines offer improved tissue interaction, reduced immune reactions, and adaptability to biologically relevant environments.[214–219] Wang et al.[215] demonstrated 3D printing of movable MSs on GelMA-based resin, followed by magnetic decoration with Fe$_2$O$_3$ NPs (10 mg mL^{-1}) for actuation (Fig. 18ai and ii). Wireless swimming tests of MSs, carried out under a rotating magnetic field, revealed variations in their swimming speed as a function of magnetic field frequency (Fig. 18aiii). The wobbling motion of MSs was observed at low frequencies (<6 Hz), with increased forward velocity of motion at higher frequencies, and then stabilizing into a corkscrew motion pattern (see Fig. 18aiii).[220] Therefore, the motion of the printed MSs was clearly demonstrated, enabling them to function as movable and remotely controlled microrobots. The mechanical softness of MSs was evaluated by measuring the storage modulus (E') of GelMA during 2PP-assisted crosslinking, demonstrating the high flexibility of the GelMA-based MSs under strong magnetic torques. The cytotoxicity and biocompatibility (Fig. 18aiv) of GelMA precursors were also investigated, showing negligible cytotoxicity and minimal impact of GelMA-based MSs on cell metabolic activity. Furthermore, the biodegradation of GelMA MSs was evaluated, revealing their rapid degradation in a collagenase solution (Fig. 18av). Biodegradation studies in human cell culture media also showed efficient GelMA MS deformation (3 days for 3T3 cells, 36 hours for HDFs cells). Control studies in cell-free culture medium demonstrated that GelMA MSs maintained their structural stability for over 16 days, highlighting the cell-mediated degradation mechanism. Consequently, these findings demonstrate the efficacy of gelatin-coated iron oxide NPs as stable and effective drug carriers, offering significant potential in biomedical applications by enabling minimally invasive procedures and precision therapies.

Biohybrid micromotors powered by sperm cells offer a promising solution for treating male infertility, especially oligospermia.[221] With external magnetic control, these micromotors can enhance sperm navigation in viscous environments, improving the likelihood of successful fertilization.[222] Striggow's group[221] fabricated a sperm-driven MS, aka spermbot, using 2PL (Fig. 18b). The spermbot demonstrated functionality in vitro within bovine oviduct fluid (BOF). Passive micro-rheology characterized BOF's viscoelastic properties, developing an artificial fluid with similar characteristics. Sperm motion parameters remained consistent in both fluids. However, the added load from magnetic microtubes caused an ON–OFF flagellar beat. To improve performance, a novel microcap (Fig. 18bi) with a parabolic outer wall and hollow beam-supported structure was introduced, enhancing tail movement while reducing mass (Fig. 18bii). The fabrication via 3D 2PL facilitated finer structural details and thinner walls compared to 2D maskless lithography, effectively reducing the mechanical load on sperm cells and improving functionality in realistic environments. The authors[221] observed that attaching a microcap to sperm disrupts its natural flagellar beat, causing a shift from a perpendicular to a parallel pattern (Fig. 18biii). They also found that viscosity affects flagellar motion, with cargo attachment leading to intermittent disruptions. The results in Fig. 18b demonstrate the effectiveness of the streamlined cap design, showcasing its successful fabrication, sperm cell integration, and magnetic guidance in BOF-EL. These findings highlight the cap's potential for precise, controlled movement in complex biological fluids, enhancing spermbot performance for biomedical applications. The study reported in ref. 221 also underscores the importance of stimuli-responsive, biodegradable materials for controlled cell release and the role of fluid dynamics and surface functionalization in optimizing micromotor performance. Addressing biological obstacles and improving navigation in viscous environments will further enhance their in vivo applicability.

Miniaturized, functional devices are key to advancing micro- and nanotechnologies. Light manipulation, particularly through optical tweezers (OTs), enables non-invasive micro-assembly and control, with applications in fluid transport and microfluidic systems.[223,224] 2PL further enhances microfluidic technology with its high resolution and design flexibility. Kohler et al.[225] presented a bottom-up assembly technique for fabricating complex

18620 | J. Mater. Chem. C, 2025, 13, 18597–18630

This journal is © The Royal Society of Chemistry 2025
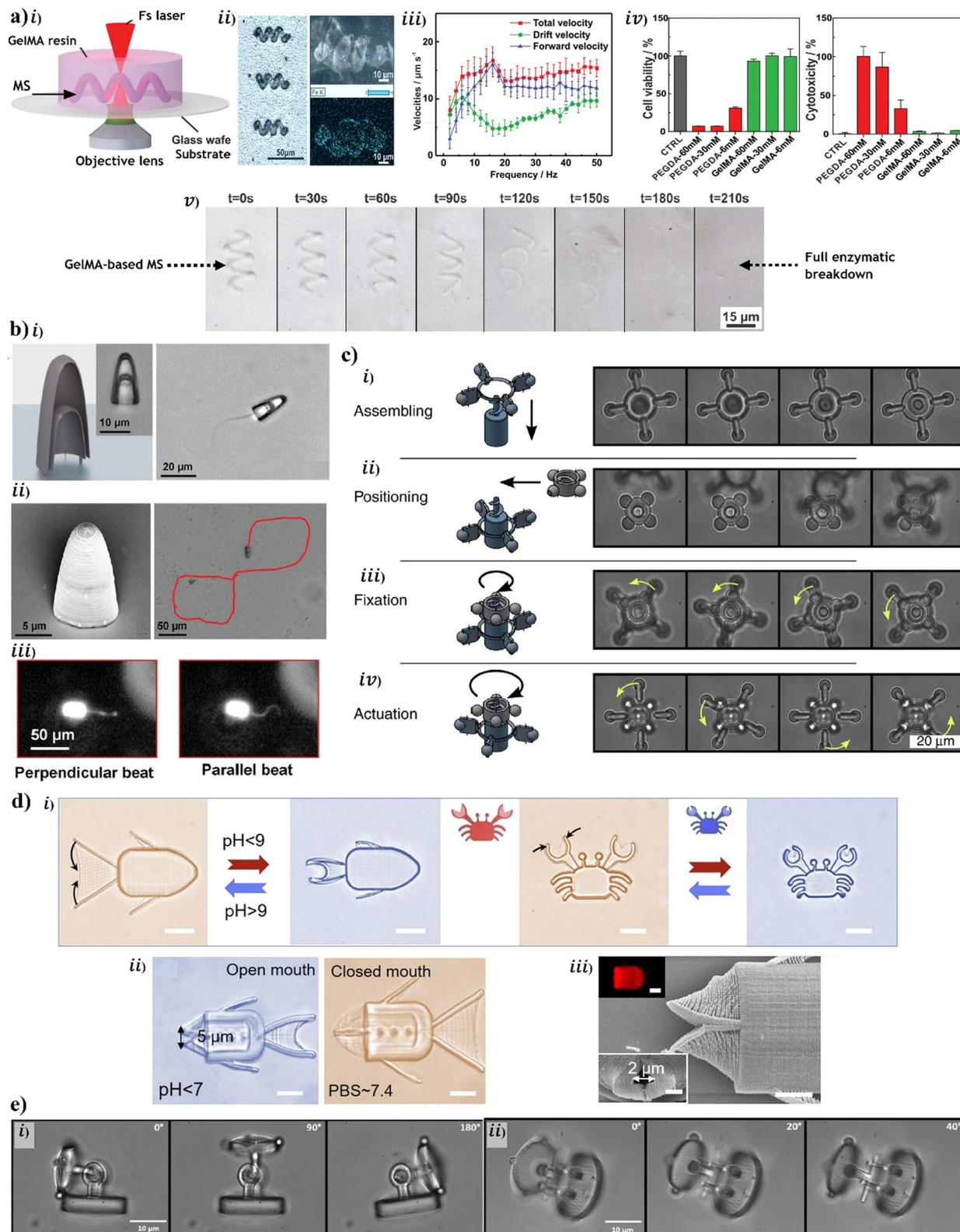
Fig. 18   2PL-based 3D printed soft microrobots for biomedical applications. (a) Mobile enzymatically microswimmers. (i) 2PP manufacturing process. (ii) Optical micrograph of MSs decorated with Fe_3O_4 NPs, and cryo-SEM, and EDX mapping of iron NPs corresponding to hydrated MSs. (iii) Swimming velocities of MSs *versus* the rotational frequency. (iv) Compatibility of MSs printed on GelMA: (left) Cell viability after one day of incubation in the mixture of GelMA and PEGDA solution, (right) Cytotoxicity of GelMA and PEGDA solutions after one day of incubation; PEGDA was used as a reference test. (v) Degradation of a GelMA-based helical MS when exposed to a 0.1 mg mL^{-1} collagenase solution. The enzymatic degradation of GelMA enables rapid breakdown in minutes (3.5 min), showing promise for transient body applications. Reproduced with permission.[215] Copyright 2018, Wiley-VCH. (b) (i) (left)

This journal is © The Royal Society of Chemistry 2025

J. Mater. Chem. C, 2025, 13, 18597–18630 | 18621

The architectural design of a hydrodynamic cap, accompanied by an optical micrograph depicting its post-release state, (right) microscopic visualization showing bovine spermatozoa successfully encapsulated within the hydrodynamic cap structure. (ii) (left) SEM micrograph revealing the detailed surface features of the hydrodynamic cap, and (right) demonstration of magnetic control capabilities for directing the hydrodynamic cap movement within BOF-EL medium. (iii) Dark-field micrographs demonstrate the mechanical influence of microcap coupling on flagellar movement, where the standard perpendicular beating transitions to a constrained parallel motion. Reproduced with permission.[221] Copyright 2020, Wiley-VCH. (c) Sequential microscope images showing the optical assembly, fixation, and actuation of the micro-rotor. (i) The rotor is trapped, aligned, and lowered onto the axis. (ii) The nut is positioned for screwing. (iii) The nut is secured, stabilizing the rotor. (iv) Optical traps rotate the rotor at ∼25 rpm rotational speed. The yellow arrows indicate the rotation direction. Reproduced under the terms of the Creative Commons License CC BY 4.0.[225] Copyright 2017, the Authors, Springer Nature. (d) (i) Optical images of an SMMF and SMMC demonstrating the pH-induced opening of fins and closing of claws, respectively. Scale bar: 25 μm. (ii) and (iii) DOX loading into an SMMF *via* mouth morphing. The SMMF's mouth remains open at pH < 7 and closes in PBS, with the red fluorescence signal indicating DOX encapsulation within the fish body. Reproduced with permission.[227] Copyright 2021, American Chemical Society (ACS). (e) Optical control of the articulated microrobot. (i) The fully mobile microrobot undergoes in-plane rotational movement of the head component by 180°, while the base remains stationary, held by two optical traps. (ii) The fully mobile microrobot performs out-of-plane rotational motion, with the head component rotating by 40°, while the base is constrained using optical traps. Reproduced with permission.[228] Copyright 2020, Wiley-VCH.

microsystems using optical methods. Their work utilized 2PL to create functional microdevices, which were then manipulated and assembled using holographic OTs (Fig. 18c). A key achievement was the development of interlocking micro-components, such as screw and nut structures, enabling stable but releasable joints. OTs served as an optical screw wrench to precisely position and assemble these microstructures at the μm-scale. This approach was validated in a microfluidic system, where a micro-rotor was assembled, secured, and actuated using optical forces. The rotor was positioned (Fig. 18ci), aligned (Fig. 18cii), fixed (Fig. 18ciii), and actuated with optical torque, achieving a rotational speed of 25 RPM for microfluidic applications (Fig. 18civ). Despite achieving lower speeds compared to other optically driven micropumps, such as those by Maruo et al.[226] performance enhancements could be realized by optimizing laser power and trapping configurations. This microscale screw connection system represents a significant advancement in microsystem integration, offering potential applications in biological research for non-toxic fixation and controlled release of cells or bacteria, as well as in microrobotics and micromechanics for force and motion transmission. Further improvements in rotational speed and system optimization are required to enhance its applicability across various microfluidic and micromechanical domains. Microassembly plays a crucial role in advancing device integration, enabling miniaturization, and expanding the boundaries of microscale technologies. Additionally, it offers significant potential in micromechanics and microbotics, particularly in applications involving biological cells, as it supports a minimally invasive control approach for various operations.

Reversible shape-morphing in nature enables self-locomotion and cargo handling.[229] Inspired by these mechanisms, millimeter-scale robots, such as artificial helix robots and magnetically actuated devices, have been developed for adaptive movement, drug delivery,[230] and cargo transport.[231] On the microscale, 2PP-fabricated robots under 100 μm size can manipulate microparticles,[62] cells,[232] and bacteria,[233] demonstrating significant potential for biomedical applications. By replicating biological principles, bionics has facilitated the advancement of printed microrobots as versatile tools for micro-object manipulation and targeted drug delivery.[227,234] To enable complex micro-/nanocargo tasks such as encapsulation and release, Xin's group[227] developed shape-morphing microrobots (SMMRs)

using pH-responsive hydrogels with programmed expansion rates (Fig. 18d). These magnetic microrobots include a shape-morphing microcrab (SMMC) (Fig. 18di) for gripping, transporting, and releasing microparticles, and a microfish (SMMF) (Fig. 18dii and iii) designed to encapsulate and release doxorubicin (DOX) in response to pH changes. A proof-of-concept study demonstrated localized HeLa cell treatment within an artificial vascular network, showcasing the potential of SMMRs for drug delivery. Zhu et al.[235] employed microscale continuous optical printing (μCOP) to fabricate a biomimetic microfish capable of encapsulating NPs, biomolecules, and living cells. Meanwhile, Xin et al.[227] developed adaptive microrobots by programming differential swelling rates in pH-responsive hydrogels, enabling pH-triggered opening and closing of claws in crab-shaped microrobots and controlled DOX release in fish-shaped microrobots. Smart millimeter-scale SMMRs offer adaptive shape transformation and remote motion control for customizable micro- and nanocargo manipulation in vitro. Their design supports applications in targeted cancer treatment, stem cell delivery, and biosensing.[236–240] Advances in size optimization, magnetic actuation, and real-time imaging could further enhance their in vivo functionality. Proof-of-concept studies have shown their potential in drug encapsulation and controlled release within artificial vascular networks, highlighting their biomedical applicability.

OTs have gained significant traction in biomedical research due to their advantages of dynamic adjustability and the ability to precisely manipulate particles in confined spaces.[241,242] Several studies have explored the concept of utilizing a rigid body as an intermediary tool in optical trapping to indirectly manipulate biological particles.[243–245] These rigid bodies typically include simple microspheres, which are cost-effective and easy to control, or nonspherical objects with spherical trapping points.[246–248] The use of rigid bodies, e.g., microrobots printed by 2PL, for indirect manipulation is a practical method for reducing the potential damage caused by direct photon irradiation. Avci et al.[228] utilized 2PL to fabricate articulated microrobots designed for the indirect manipulation of cellular structures under laser illumination (Fig. 18e). They demonstrated a methodology for fabricating and controlling untethered articulated microrobots using light force, achieving the first optical manipulation of a floating, multi-component micro-mechanism. This breakthrough is expected to

18622 | J. Mater. Chem. C, 2025, 13, 18597–18630

This journal is © The Royal Society of Chemistry 2025

have great promise for advanced biomedical applications requiring precise 3D control, including single-cell analysis, embryo injection, polar-body biopsy, nuclear transplantation, and micro-surgery imaging. Avci's group[228] also explored the design, fabrication, and control of a mobile articulated microrobot for dexterous cell handling using laser beam manipulation. The microrobot was designed to convert in-plane laser trap motion into out-of-plane rotation (Fig. 18e). A simple articulated mechanism with a single joint and minimal contact points addressed adhesion challenges at the microscale. The untethered microrobot demonstrated 180° in-plane motion (Fig. 18ei) and up to 40° out-of-plane rotations (Fig. 18eii) using two optical trap points to immobilize the base and rotate the mobile head. This represents a significant advancement in optical manipulation. The articulated microrobots have the potential to be applied in advanced biomedical fields that demand precise 3D control, such as single-cell analysis, embryo injection, polar-body biopsy, nuclear transplantation, and multi-dimensional microsurgical imaging.

2PP-assisted 3D lithography has proven to be a powerful technique for fabricating complex microstructures with sub-micron precision, enabling the creation of soft, functional micro-robots for various biomedical applications. These microrobots demonstrated exceptional biocompatibility, responsiveness, and adaptability, making them ideal for targeted drug delivery, minimally invasive surgery, and tissue engineering. Future advancements in materials, including stimuli-responsive polymers, will further enhance their actuation and sensing capabilities. Integration with wireless control systems and real-time imaging will further improve their navigation and operational efficiency. While scalability and mass production remain challenges, interdisciplinary efforts in nanophotonics, bioengineering, and robotics will drive innovations. Ultimately, 2PP-printed soft microrobots are promising to revolutionize personalized and precision medicine.

7. Challenges and opportunities

2PL is widely recognized for its unique ability to fabricate complex 3D micro- and nanostructures with SDL resolution. However, several technical and practical limitations currently hinder its widespread industrial deployment. One major challenge is the inherently serial nature of voxel-by-voxel printing, which restricts throughput and makes the process time-intensive for large-scale structures and high-volume production. This limitation becomes even more pronounced when high-resolution printing is required over complex or centimeter-scale areas. This is due to the imposed relationship between resolution and throughput, which follows a third-power law in 3D systems.[164] Another significant constraint lies in the limited working volume, dictated by the use of high NA OL, which reduces the effective print field and complicates the fabrication of macroscale devices. While stitching techniques can extend the working area, they often introduce alignment errors and structural discontinuities. Moreover, the high cost of 2PP printing systems, primarily driven by the price of the Fs lasers, adds to the economic barrier of deploying 2PP for commercial production. Material compatibility also remains a

concern. The available photoresists that exhibit both strong 2PA and desirable mechanical, optical, or biofunctional properties are limited, which narrows the range of application-specific materials. Additionally, long design-to-print cycles, driven by the need for manual optimization and lack of real-time feedback, reduce efficiency and increase the trial-and-error workload. These challenges highlight the need for modern technological advances, including improved laser sources, optical systems, materials, and automation tools. These advances are discussed below in this section.

In the past five years, considerable research efforts have been devoted to enhancing throughput, reducing the size and cost of 2PL systems, and developing advanced multifunctional materials. Notable improvements in throughput have been achieved through the integration of parallelized optical systems, such as microlens arrays (MLAs) and more recently, diffractive optical elements (DOEs), which facilitate the simultaneous generation of multiple focal points.[28,81] However, while these parallelization strategies substantially accelerate the fabrication process, their inherent static nature prevents individual control of each focus, thus confining their use to the fabrication of periodic structures. To overcome this limitation, dynamic beam modulation strategies, such as those based on spatial light modulators (SLMs)[249] and digital micromirror devices (DMDs),[250] have emerged as promising alternatives. These holography-based approaches allow the fabrication of complex and arbitrary 3D architectures, by enabling real-time control over the position and intensity of individual foci. A recent advancement in this area demonstrated the use of a holography-assisted DMD scanner capable of generating up to 2000 dynamically programmable foci, enabling the high-throughput fabrication of complex 3D microstructures and large-scale areas (up to 4 cm^2) with fine resolution down to 90 nm.[251] More recently, some studies have raised the possibility of using holography-based single spatiotemporally shaped pulse approaches to print macroscopic 3D structures with nanoscale features at the speed of light, typically in the order of 10^{20}–10^{21} voxels per s.[70,252] This cutting-edge approach could revolutionize 2PL, positioning it as a transformative technology for ultra-fast, high-resolution 3D nanomanufacturing.

Recent developments in scanning systems have significantly progressed 2PL speed capabilities. The integration of synchronized linear stages with galvanometric scanners has enabled continuous, stitch-free fabrication over extended areas (up to tens-of-cm) at high translation speeds up to cm s^{-1}, while preserving nanoscale positioning accuracy and print integrity.[101] In parallel, the use of state-of-the-art polygon scanners has facilitated ultrafast scanning at 10 m s^{-1} velocities, considerably enhancing processing speed.[253] In addition, two-photon grayscale lithography (2GL) has emerged as a transformative method, leveraging rapid laser intensity modulation through acousto-optic modulators (AOMs) to dynamically adjust voxel dimensions. This has enabled 3D microfabrication of precise, distortion-free complex geometries with substantially elevated throughput, eliminating the need for traditional layer-by-layer slicing.[254,255]

Unlike costly Fs lasers, more affordable and compact pico-second pulsed sources, such as microchip lasers and monolithic

laser diodes, offer a cost-effective alternative while maintaining sufficient performance for a range of applications.[256,257] More recently, researchers have demonstrated the fabrication of 2D/3D microstructures using a CW laser diode, surpassing prior benchmarks typically achieved with Fs laser systems.[67] This was made possible through a two-step absorption mechanism that replaces the traditional virtual state (lifetime $\sim$ 100 fs) with a long-lived real state ($\sim$ 100 ms), allowing the efficient sequential absorption of two photons using only $\sim$ 100 μW CW-laser power. This innovative strategy enables the development of highly compact and cost-efficient 2PP printing systems, with footprints under 50 cm and costs reduced to just tens of US dollars. Current development efforts focus on leveraging this technique to reach ultrafast printing speeds by integrating principles from light sheet microscopy.[258]

Advancements in materials science, such as the development of ultrasensitive photoresists, stimuli-responsive smart materials, and hybrid or nanocomposite formulations – are significantly broadening the functional versatility of 2PL across a wide range of applications.[7,8,105] In addition, the emergence of multi-material printing further enables the fabrication of intricate heterogeneous microdevices tailored to diverse application fields.[259,260]

Parallel to these advances, the recent integration of machine learning (ML) and AI is revolutionizing 2PP manufacturing by accelerating process optimization and minimizing manufacturing errors. AI-driven algorithms now can efficiently determine optimal printing parameters, such as exposure protocols, scan overlap and model pre-compensation, for diverse materials and geometries. This significantly minimizes manual calibration and reduces the need for trial-and-error iterations, thereby shortening the overall fabrication time and mitigating manufacturing errors associated with materials and laser processing conditions.[66,261–263] In addition, integrating AI with *in situ* characterization and other advanced techniques promises enhanced spatial precision and quality, real-time defect correction, and precise modulation of exposure levels.[264] As these computational methods mature, they are expected to push 2PL toward its theoretical manufacturing frontiers, improving scalability, reproducibility, and resolution, which will ultimately revolutionize industrial 2PL nanomanufacturing.

Collectively, these emerging advancements, though still in early stages of development, have significant potential to transition 2PL from a laboratory prototyping technique to a robust industrial-scale manufacturing platform.

8. Conclusion and perspectives

Two photon 3D printing is a branch of nanophotonics that has emerged as a transformative technology, enabling the manufacture of intricate, multifunctional microdevices that offer revolutionary applications in a variety of sectors. It stands out for its ability to create complex 3D microstructures with resolutions well below the optical diffraction limit, leveraged by the NL 2PA effect. Unlike traditional photolithography, 2PL offers

the advantage of precise fabrication in 3D, without the use of masks and under ambient conditions, enabling the manufacture of complex microdevices that were previously unfeasible. This review has provided a comprehensive overview of 2PL, covering its basic principles, experimental aspects, and various functional 2PA photosensitive materials. It also highlighted the extensive applications of 2PL, including its role in developing multifunctional microdevices for applications in micro-optics and imaging, microelectronics/micro-optoelectronics, and biomedicine. In addition, the theoretical aspects underlying the exceptional feature resolution of the printed microstructures, as well as various innovative strategies for enhancing throughput, resolution and accuracy of 2PL, were reviewed.

Despite the progress made in 2PL, several challenges remain. Fundamental physical limitations, such as optical diffraction and material response, continue to constrain further miniaturization and resolution. Slow printing speeds limit the overall throughput, especially for fabricating highly complex 3D microstructures. Additionally, achieving consistent manufacturing on a large scale remains a bottleneck, particularly for commercial applications. However, collaborative research efforts and the development of innovative functional materials, advanced scanning systems, adaptive optics, and optimized exposure strategies show promise for overcoming these challenges. Hybridization of 2PL with other lithography methods, such as UV, nanoimprint, and interference lithography, also promises to further enhance 2PL performance by increasing design flexibility, reducing processing time, and enabling multi-scale manufacturing. Furthermore, the integration of machine learning algorithms (*e.g.*, AI-automated parameter optimization and prediction of optimized material properties) and innovative strategies, such as parallel processing (multi-beam printing) and RAPID/STED techniques, are expected to significantly improve the processing speed, reproducibility and resolution of 2PL. Looking forward, the future of 2PL is bright, with the potential to revolutionize sectors such as optoelectronics, biomedicine, micro-optics, and medical microrobotics. Ongoing improvements in resolution, throughput, scalability, and material versatility will further expand the range of feasible applications. In conclusion, although 2PL has made significant strides, its full potential has yet to be realized. By addressing current challenges and pushing the boundaries of nanoscale manufacturing, 2PL will play a crucial role as a platform technology for the development of the next generation of micro- and nanoscale devices that will offer transformative solutions in various scientific and industrial fields.

Author contributions

Conceptualization, Visualization, Writing – original draft: I. B. and Y. B.; both authors jointly wrote the manuscript, prepared the figures, and reviewed and approved the final version of this review paper.

Conflicts of interest

The authors declare no conflicts of interest.

18624 | *J. Mater. Chem. C*, 2025, **13**, 18597–18630

This journal is © The Royal Society of Chemistry 2025

Data availability

This article is a review and does not include any new data. All information discussed is based on previously published studies, which are cited appropriately in the manuscript.

Acknowledgements

References

1 C. Miller, *Chip War: The Fight for the World's Most Critical Technology*, Simon and Schuster, 2022.

2 Z. Cui, *Nanofabrication: Principles, Capabilities and Limits*, Springer, Cham, 2024.

3 M. Farsari and B. N. Chichkov, *Nat. Photonics*, 2009, **3**, 450–452.

4 S.-H. Park, D.-Y. Yang and K.-S. Lee, *Laser Photonics Rev.*, 2009, **3**, 1–11.

5 Y.-L. Zhang, Q.-D. Chen, H. Xia and H.-B. Sun, *Nano Today*, 2010, **5**, 435–448.

6 V. Harinarayana and Y. C. Shin, *Opt. Laser Technol.*, 2021, **142**, 107180.

7 S.-F. Liu, Z.-W. Hou, L. Lin, Z. Li and H.-B. Sun, *Adv. Funct. Mater.*, 2023, **33**, 2211280.

8 A. Jaiswal, C. K. Rastogi, S. Rani, G. P. Singh, S. Saxena and S. Shukla, *iScience*, 2023, **26**, 106374.

9 H.-B. Sun and S. Kawata, *J. Light Technol.*, 2003, **21**, 624.

10 A. Ovsianikov and B. N. Chichkov, in *Nanoelectronics and Photonics: From Atoms to Materials, Devices, and Architectures*, ed. A. Korkin and F. Rosei, Springer, New York, NY, 2008, pp. 427–446.

11 S. Maruo, O. Nakamura and S. Kawata, *Opt. Lett.*, 1997, **22**, 132–134.

12 S. Kawata, H.-B. Sun, T. Tanaka and K. Takada, *Nature*, 2001, **412**, 697–698.

13 V. Hahn, F. Mayer, M. Thiel and M. Wegener, *Opt. Photonics News*, 2019, **30**, 28–35.

14 Z. Sekkat and S. Kawata, *Laser Photonics Rev.*, 2014, **8**, 1–26.

15 Z. Faraji Rad, P. D. Prewett and G. J. Davies, *Microsyst. Nanoeng.*, 2021, **7**, 1–17.

16 H.-B. Sun and S. Kawata, *Adv. Polym. Sci.*, 2006, **170**, 169–273.

17 J. T. Fourkas, in *Three-Dimensional Microfabrication Using Two-Photon Polymerization*, ed. T. Baldacchini, William Andrew Publishing, 2020, pp. 57–76.

18 W. Haske, V. W. Chen, J. M. Hales, W. Dong, S. Barlow, S. R. Marder and J. W. Perry, *Opt. Express*, 2007, **15**, 3426–3436.

19 Y. Bougdid and Z. Sekkat, *Sci. Rep.*, 2020, **10**, 10409.

20 Y. Bougdid, I. Maouli, A. Rahmouni, K. Mochizuki, I. Bennani, M. Halim and Z. Sekkat, *J. Micromech. Microeng.*, 2019, **29**, 035018.

21 X. Zhou, Y. Hou and J. Lin, *AIP Adv.*, 2015, **5**, 030701.

22 Z. Huang, G. C.-P. Tsui, Y. Deng and C.-Y. Tang, *Nanotechnol. Rev.*, 2020, **9**, 1118–1136.

23 S. O'Halloran, A. Pandit, A. Heise and A. Kellett, *Adv. Sci.*, 2023, **10**, 2204072.

24 X. Wang, Z. Wei, C. Zuwu Baysah, M. Zheng and J. Xing, *RSC Adv.*, 2019, **9**, 34472–34480.

25 J. Serbin, A. Egbert, A. Ostendorf, B. N. Chichkov, R. Houbertz, G. Domann, J. Schulz, C. Cronauer, L. Fröhlich and M. Popall, *Opt. Lett.*, 2003, **28**, 301–303.

26 S. Steenhusen, F. Burmeister, H.-C. Eckstein and R. Houbertz, *Laser 3D Manufacturing II*, SPIE, 2015, vol. 9353, pp. 59–67.

27 B. Lebeau and P. Innocenzi, *Chem. Soc. Rev.*, 2011, **40**, 886–906.

28 J. Kato, N. Takeyasu, Y. Adachi, H.-B. Sun and S. Kawata, *Appl. Phys. Lett.*, 2005, **86**, 044102.

29 C. N. LaFratta and L. Li, in *Three-Dimensional Microfabrication Using Two-Photon Polymerization*, ed. T. Baldacchini, William Andrew Publishing, 2nd edn, 2020, pp. 385–408.

30 A. Taguchi, A. Nakayama, R. Oketani, S. Kawata and K. Fujita, *ACS Appl. Nano Mater.*, 2020, **3**, 11434–11441.

31 K. Parkatzidis, E. Kabouraki, A. Selimis, M. Kaliva, A. Ranella, M. Farsari and M. Vamvakaki, *Macromol. Mater. Eng.*, 2018, **303**, 1800458.

32 A. Grabulosa, J. Moughames, X. Porte and D. Brunner, *Nanophotonics*, 2022, **11**, 1591–1601.

33 W. Zhang, L.-H. Han and S. Chen, *J. Manuf. Sci. Eng.*, 2010, **132**, 030907.

34 V. Mohanavel, G. Gandhimathi, D. Bhardwaj, M. Kavitha, G. Ramkumar, M. V. Ishwarya and M. Ali, *Opt. Quantum Electron.*, 2023, **56**, 210.

35 B. Wang, P. Wang, J. Song, Y. C. Lam, H. Song, Y. Wang and S. Liu, *J. Mater. Process. Technol.*, 2022, **308**, 117716.

36 R. Pingali and S. K. Saha, *J. Manuf. Sci. Eng.*, 2021, **144**, 021011.

37 A. N. Bakhtiyari, Z. Wang, L. Wang and H. Zheng, *Opt. Laser Technol.*, 2021, **135**, 106721.

38 C. Schizas, V. Melissinaki, A. Gaidukeviciute, C. Reinhardt, C. Ohrt, V. Dedoussis, B. N. Chichkov, C. Fotakis, M. Farsari and D. Karalekas, *Int. J. Adv. Manuf. Technol.*, 2010, **48**, 435–441.

39 I. S. Ladner, M. A. Cullinan and S. K. Saha, *RSC Adv.*, 2019, **9**, 28808–28813.

40 V. P. Stinson, S. Park, M. McLamb, G. Boreman and T. Hofmann, *Optics*, 2021, **2**, 284–291.

41 G. von Freymann, A. Ledermann, M. Thiel, I. Staude, S. Essig, K. Busch and M. Wegener, *Adv. Funct. Mater.*, 2010, **20**, 1038–1052.

42 C. A. Koepele, M. Guix, C. Bi, G. Adam and D. J. Cappelleri, *Adv. Intell. Syst.*, 2020, **2**, 1900147.

43 T. Gissibl, S. Thiele, A. Herkommer and H. Giessen, *Nat. Photonics*, 2016, **10**, 554–560.

44 F. Kotz, A. S. Quick, P. Risch, T. Martin, T. Hoose, M. Thiel, D. Helmer and B. E. Rapp, *Adv. Mater.*, 2021, **33**, 2006341.

This journal is © The Royal Society of Chemistry 2025

J. Mater. Chem. C, 2025, **13**, 18597–18630 | **18625**

45 U. Bozuyuk, O. Yasa, I. C. Yasa, H. Ceylan, S. Kizilel and M. Sitti, *ACS Nano*, 2018, **12**, 9617–9625.

46 H. Wang, W. Zhang, D. Ladika, H. Yu, D. Gailevičius, H. Wang, C.-F. Pan, P. N. S. Nair, Y. Ke, T. Mori, J. Y. E. Chan, Q. Ruan, M. Farsari, M. Malinauskas, S. Juodkazis, M. Gu and J. K. W. Yang, *Adv. Funct. Mater.*, 2023, **33**, 2214211.

47 M. Malinauskas, M. Farsari, A. Piskarskas and S. Juodkazis, *Phys. Rep.*, 2013, **533**, 1–31.

48 X. Hu, I. C. Yasa, Z. Ren, S. R. Goudu, H. Ceylan, W. Hu and M. Sitti, *Sci. Adv.*, 2021, **7**, eabe8436.

49 G. van der Velden, D. Fan and U. Staufer, *Micro Nano Eng.*, 2020, **7**, 100054.

50 M. Suter, L. Zhang, E. C. Siringil, C. Peters, T. Luehmann, O. Ergeneman, K. E. Peyer, B. J. Nelson and C. Hierold, *Biomed. Microdevices*, 2013, **15**, 997–1003.

51 M. Deubel, G. von Freymann, M. Wegener, S. Pereira, K. Busch and C. M. Soukoulis, *Nat. Mater.*, 2004, **3**, 444–447.

52 A. Ovsianikov, S. Schlie, A. Ngezahayo, A. Haverich and B. N. Chichkov, *J. Tissue Eng. Regener. Med.*, 2007, **1**, 443–449.

53 https://www.nanoscribe.com/en/, accessed May 11, 2025.

54 https://heidelberg-instruments.com/multiphoton-optics-becomes-branch-office/, accessed may 11, 2025.

55 M. Göppert-Mayer, *Ann. Phys.*, 1931, **401**, 273–294.

56 W. Kaiser and C. G. B. Garrett, *Phys. Rev. Lett.*, 1961, **7**, 229–231.

57 Y.-H. Pao and P. M. Rentzepis, *Appl. Phys. Lett.*, 1965, **6**, 93–95.

58 B. H. Cumpston, S. P. Ananthavel, S. Barlow, D. L. Dyer, J. E. Ehrlich, L. L. Erskine, A. A. Heikal, S. M. Kuebler, I.-Y. S. Lee, D. McCord-Maughon, J. Qin, H. Röckel, M. Rumi, X.-L. Wu, S. R. Marder and J. W. Perry, *Nature*, 1999, **398**, 51–54.

59 A. Doraiswamy, C. Jin, R. J. Narayan, P. Mageswaran, P. Mente, R. Modi, R. Auyeung, D. B. Chrisey, A. Ovsianikov and B. Chichkov, *Acta Biomater.*, 2006, **2**, 267–275.

60 L. Li, R. R. Gattass, E. Gershgoren, H. Hwang and J. T. Fourkas, *Science*, 2009, **324**, 910–913.

61 J. Fischer, G. von Freymann and M. Wegener, *Adv. Mater.*, 2010, **22**, 3578–3582.

62 S. Tottori, L. Zhang, F. Qiu, K. K. Krawczyk, A. Franco-Obregón and B. J. Nelson, *Adv. Mater.*, 2012, **24**, 811–816.

63 Z. Gan, Y. Cao, R. A. Evans and M. Gu, *Nat. Commun.*, 2013, **4**, 2061.

64 W. Xiong, Y. Liu, L. J. Jiang, Y. S. Zhou, D. W. Li, L. Jiang, J.-F. Silvain and Y. F. Lu, *Adv. Mater.*, 2016, **28**, 2002–2009.

65 https://www.nanoscribe.com/en/news-insights/press-releases/nanoscribe-launches-quantum-x-for-the-fabrication-of-highly-precise-microoptics/, accessed July 18, 2025.

66 X. Y. Lee, S. K. Saha, S. Sarkar and B. Giera, *Addit. Manuf.*, 2020, **36**, 101444.

67 V. Hahn, T. Messer, N. M. Bojanowski, E. R. Curticean, I. Wacker, R. R. Schröder, E. Blasco and M. Wegener, *Nat. Photonics*, 2021, **15**, 932–938.

68 https://www.nanoscribe.com/en/news-insights/news/3d-printing-by-2gl/, accessed July 18, 2025.

69 P. Kiefer, V. Hahn, S. Kalt, Q. Sun, Y. M. Eggeler and M. Wegener, *Light Adv. Manuf.*, 2024, **4**, 28–41.

70 M. Wegener and P. Somers, *Advanced Fabrication Technologies for Micro/Nano Optics and Photonics XVIII*, SPIE, 2025, vol. 13381, p. PC133810H.

71 Y. R. Shen, *The Principles of Nonlinear Optics*, Wiley, 2003.

72 R. Menzel, *Photonics: Linear and Nonlinear Interactions of Laser Light and Matter*, Springer Berlin, Heidelberg, 2nd edn, 2007.

73 K.-S. Lee, R. H. Kim, D.-Y. Yang and S. H. Park, *Prog. Polym. Sci.*, 2008, **33**, 631–681.

74 W. R. Zipfel, R. M. Williams and W. W. Webb, *Nat. Biotechnol.*, 2003, **21**, 1369–1377.

75 J. J. Hopfield, J. M. Worlock and K. Park, *Phys. Rev. Lett.*, 1963, **11**, 414–417.

76 D. Fröhlich, in *Nonlinear Spectroscopy of Solids: Advances and Applications*, ed. B. D. Bartolo, Springer US, Boston, MA, 1994, pp. 289–326.

77 A. S. Dvornikov, E. P. Walker and P. M. Rentzepis, *J. Phys. Chem. A*, 2009, **113**, 13633–13644.

78 W. Denk, J. H. Strickler and W. W. Webb, *Science*, 1990, **248**, 73–76.

79 P. Kiefer, V. Hahn, M. Nardi, L. Yang, E. Blasco, C. Barner-Kowollik and M. Wegener, *Adv. Opt. Mater.*, 2020, **8**, 2000895.

80 A. Vyatskikh, R. C. Ng, B. Edwards, R. M. Briggs and J. R. Greer, *Nano Lett.*, 2020, **20**, 3513–3520.

81 V. Hahn, P. Kiefer, T. Frenzel, J. Qu, E. Blasco, C. Barner-Kowollik and M. Wegener, *Adv. Funct. Mater.*, 2020, **30**, 1907795.

82 K. Sugioka and Y. Cheng, *Appl. Phys. Rev.*, 2014, **1**, 041303.

83 I. Wang, M. Bouriau, P. L. Baldeck, C. Martineau and C. Andraud, *Opt. Lett.*, 2002, **27**, 1348–1350.

84 M. Rumi and J. W. Perry, *Adv. Opt. Photon.*, 2010, **2**, 451–518.

85 K. J. Schafer, J. M. Hales, M. Balu, K. D. Belfield, E. W. Van Stryland and D. J. Hagan, *J. Photochem. Photobiol. Chem.*, 2004, **162**, 497–502.

86 R. Menzel, *Photonics*, Springer, Berlin, Heidelberg, 2007, pp. 93–171.

87 R. Menzel, *Photonics*, Springer Berlin Heidelberg, Berlin, Heidelberg, 2007, pp. 263–358.

88 R. L. Sutherland, *Handbook of Nonlinear Optics*, CRC Press, 2nd edn, 2003.

89 M. Sheik-Bahae, A. A. Said, T.-H. Wei, D. J. Hagan and E. W. Van Stryland, *IEEE J. Quantum Electron.*, 1990, **26**, 760–769.

90 M. Bass, E. W. Van Stryland, D. R. Williams and W. L. Wolfe, *Handbook of Optics: Fundamentals, techniques, and design*, McGraw-Hill Professional, O. S. America, 2nd edn, 1995, vol. 1.

91 A. Bagheri and J. Jin, *ACS Appl. Polym. Mater.*, 2019, **1**, 593–611.

92 E. Skliutas, M. Lebedevaite, E. Kabouraki, T. Baldacchini, J. Ostrauskaite, M. Vamvakaki, M. Farsari, S. Juodkazis and M. Malinauskas, *Nanophotonics*, 2021, **10**, 1211–1242.

93 J. Kabatc, J. Ortyl and K. Kostrzewska, *RSC Adv.*, 2017, **7**, 41619–41629.

18626 | *J. Mater. Chem. C*, 2025, **13**, 18597–18630

This journal is © The Royal Society of Chemistry 2025

94 S. Wu, J. Serbin and M. Gu, *J. Photochem. Photobiol. Chem.*, 2006, **181**, 1–11.

95 Z. Sekkat, I. Boudene and S. Refki, *J. Phys. Chem. C*, 2023, **127**, 11378–11386.

96 A. Rahmouni, Y. Bougdid, S. Moujdi, D. V. Nesterenko and Z. Sekkat, *J. Phys. Chem. B*, 2016, **120**, 11317–11322.

97 O. Lugier, N. Thakur, L. Wu, M. Vockenhuber, Y. Ekinci and S. Castellanos, *ACS Appl. Mater. Interfaces*, 2021, **13**, 43777–43786.

98 D. Kazazis, J. G. Santaclara, J. van Schoot, I. Mochi and Y. Ekinci, *Nat. Rev. Methods Primer*, 2024, **4**, 1–15.

99 C. Zhu, H. Ekinci, A. Pan, B. Cui and X. Zhu, *Microsyst. Nanoeng.*, 2024, **10**, 1–23.

100 S. Maruo, in *Handbook of Laser Micro- and Nano-Engineering*, ed. K. Sugioka, Springer International Publishing, Cham, 2020, pp. 1–25.

101 L. Jonušauskas, D. Gailevičius, S. Rekštytė, T. Baldacchini, S. Juodkazis and M. Malinauskas, *Opt. Express*, 2019, **27**, 15205–15221.

102 T. Tanaka, H.-B. Sun and S. Kawata, *Appl. Phys. Lett.*, 2002, **80**, 312–314.

103 Y. Lu, F. Hasegawa, T. Goto, S. Ohkuma, S. Fukuhara, Y. Kawazu, K. Totani, T. Yamashita and T. Watanabe, *J. Mater. Chem.*, 2004, **14**, 75–80.

104 W. Zhou, S. M. Kuebler, K. L. Braun, T. Yu, J. K. Cammack, C. K. Ober, J. W. Perry and S. R. Marder, *Science*, 2002, **296**, 1106–1109.

105 M. Carlotti and V. Mattoli, *Small*, 2019, **15**, 1902687.

106 G. Witzgall, R. Vrijen, E. Yablonovitch, V. Doan and B. J. Schwartz, *Opt. Lett.*, 1998, **23**, 1745–1747.

107 W. H. Teh, U. Dürig, G. Salis, R. Harbers, U. Drechsler, R. F. Mahrt, C. G. Smith and H.-J. Güntherodt, *Appl. Phys. Lett.*, 2004, **84**, 4095–4097.

108 L. H. Nguyen, M. Straub and M. Gu, *Adv. Funct. Mater.*, 2005, **15**, 209–216.

109 S. Ushiba, K. Masui, N. Taguchi, T. Hamano, S. Kawata and S. Shoji, *Sci. Rep.*, 2015, **5**, 17152.

110 H.-B. Sun, S. Matsuo and H. Misawa, *Appl. Phys. Lett.*, 1999, **74**, 786–788.

111 S. Wu, M. Straub and M. Gu, *Polymer*, 2005, **46**, 10246–10255.

112 A.-I. Bunea, N. del Castillo Iniesta, A. Droumpali, A. E. Wetzel, E. Engay and R. Taboryski, *Micro*, 2021, **1**, 164–180.

113 https://www.nanoscribe.com/en/products/ip-photoresins/, accessed May 11, 2025.

114 M. Kadic, G. W. Milton, M. van Hecke and M. Wegener, *Nat. Rev. Phys.*, 2019, **1**, 198–210.

115 A. Ovsianikov, M. Malinauskas, S. Schlie, B. Chichkov, S. Gittard, R. Narayan, M. Löbler, K. Sternberg, K.-P. Schmitz and A. Haverich, *Acta Biomater.*, 2011, **7**, 967–974.

116 J. D. Pitts, P. J. Campagnola, G. A. Epling and S. L. Goodman, *Macromolecules*, 2000, **33**, 1514–1523.

117 M. Farsari, M. Vamvakaki and B. N. Chichkov, *J. Opt.*, 2010, **12**, 124001.

118 J. Wang, H. Xia, B.-B. Xu, L.-G. Niu, D. Wu, Q.-D. Chen and H.-B. Sun, *Opt. Lett.*, 2009, **34**, 581–583.

119 D. W. Yee, M. L. Lifson, B. W. Edwards and J. R. Greer, *Adv. Mater.*, 2019, **31**, 1901345.

120 Y. Peng, S. Jradi, X. Yang, M. Dupont, F. Hamie, X. Q. Dinh, X. W. Sun, T. Xu and R. Bachelot, *Adv. Mater. Technol.*, 2019, **4**, 1800522.

121 Y. Liu, W. Xiong, D. W. Li, Y. Lu, X. Huang, H. Liu, L. S. Fan, L. Jiang, J.-F. Silvain and Y. F. Lu, *Int. J. Extreme Manuf.*, 2019, **1**, 025001.

122 Y. Liu, W. Xiong, L. J. Jiang, Y. S. Zhou and Y. F. Lu, *in Laser 3D Manufacturing III*, SPIE, 2016, vol. 9738, pp. 21–29.

123 H. Xia, J. Wang, Y. Tian, Q.-D. Chen, X.-B. Du, Y.-L. Zhang, Y. He and H.-B. Sun, *Adv. Mater.*, 2010, **22**, 3204–3207.

124 Y. Xia, Y. He, F. Zhang, Y. Liu and J. Leng, *Adv. Mater.*, 2021, **33**, 2000713.

125 W. Zhang, H. Wang, H. Wang, J. Y. E. Chan, H. Liu, B. Zhang, Y.-F. Zhang, K. Agarwal, X. Yang, A. S. Ranganath, H. Y. Low, Q. Ge and J. K. W. Yang, *Nat. Commun.*, 2021, **12**, 112.

126 X. Wen, B. Zhang, W. Wang, F. Ye, S. Yue, H. Guo, G. Gao, Y. Zhao, Q. Fang, C. Nguyen, X. Zhang, J. Bao, J. T. Robinson, P. M. Ajayan and J. Lou, *Nat. Mater.*, 2021, **20**, 1506–1511.

127 A. Vyatskikh, S. Delalande, A. Kudo, X. Zhang, C. M. Portela and J. R. Greer, *Nat. Commun.*, 2018, **9**, 593.

128 C. N. LaFratta, J. T. Fourkas, T. Baldacchini and R. A. Farrer, *Angew. Chem., Int. Ed.*, 2007, **46**, 6238–6258.

129 L. Li and J. T. Fourkas, *Mater. Today*, 2007, **10**, 30–37.

130 R. A. Farrer, C. N. LaFratta, L. Li, J. Praino, M. J. Naughton, B. E. A. Saleh, M. C. Teich and J. T. Fourkas, *J. Am. Chem. Soc.*, 2006, **128**, 1796–1797.

131 S. Maruo and T. Saeki, *Opt. Express*, 2008, **16**, 1174–1179.

132 T. Tanaka, A. Ishikawa and S. Kawata, *Appl. Phys. Lett.*, 2006, **88**, 081107.

133 E. Blasco, J. Müller, P. Müller, V. Trouillet, M. Schön, T. Scherer, C. Barner-Kowollik and M. Wegener, *Adv. Mater.*, 2016, **28**, 3592–3595.

134 C. L. Lay, C. S. L. Koh, Y. H. Lee, G. C. Phan-Quang, H. Y. F. Sim, S. X. Leong, X. Han, I. Y. Phang and X. Y. Ling, *ACS Appl. Mater. Interfaces*, 2020, **12**, 10061–10079.

135 T. Baldacchini, C. N. LaFratta, R. A. Farrer, M. C. Teich, B. E. A. Saleh, M. J. Naughton and J. T. Fourkas, *J. Appl. Phys.*, 2004, **95**, 6072–6076.

136 S. Engelhardt, E. Hoch, K. Borchers, W. Meyer, H. Krüger, G. E. M. Tovar and A. Gillner, *Biofabrication*, 2011, **3**, 025003.

137 K. D. Belfield, K. J. Schafer, Y. Liu, J. Liu, X. Ren and E. W. V. Stryland, *J. Phys. Org. Chem.*, 2000, **13**, 837–849.

138 E. Abbe, *Arch. Mikrosk. Anat. Entwicklungsmech.*, 1873, **9**, 413–468.

139 C. Wagner and N. Harned, *Nat. Photonics*, 2010, **4**, 24–26.

140 J. Fischer and M. Wegener, *Laser Photonics Rev.*, 2013, **7**, 22–44.

141 Ch. J. Schwarz, A. V. V. Nampoothiri, J. C. Jasapara, W. Rudolph and S. R. J. Brueck, *J. Vac. Sci. Technol., B: Microelectron. Nanometer Struct.--Process., Meas., Phenom.*, 2001, **19**, 2362–2365.

142 G. de Miguel, G. Vicidomini, B. Harke and A. Diaspro, in *Three-Dimensional Microfabrication Using Two-photon*

This journal is © The Royal Society of Chemistry 2025

J. Mater. Chem. C, 2025, **13**, 18597–18630 | **18627**

Polymerization, ed. T. Baldacchini, William Andrew Publishing, Oxford, 2016, pp. 190–220.

143 P. J. Flory, *Principles of Polymer Chemistry*, Cornell University Press, New York, 1953.

144 Y. Bougdid, I. Maouli, A. Rahmouni, K. Mochizuki, M. Halim and Z. Sekkat, *Molecular Machines*, SPIE, 2018, vol. 10740, pp. 28–32.

145 S. Juodkazis, V. Mizeikis, K. K. Seet, M. Miwa and H. Misawa, *Nanotechnology*, 2005, **16**, 846.

146 M. V. Rybin, I. I. Shishkin, K. B. Samusev, P. A. Belov, Y. S. Kivshar, R. V. Kiyan, B. N. Chichkov and M. F. Limonov, *Crystals*, 2015, **5**, 61–73.

147 J.-F. Xing, X.-Z. Dong, W.-Q. Chen, X.-M. Duan, N. Takeyasu, T. Tanaka and S. Kawata, *Appl. Phys. Lett.*, 2007, **90**, 131106.

148 T. Baldacchini, *Three-Dimensional Microfabrication Using Two-Photon Polymerization: Fundamentals, Technology, and Applications*, Elsevier Science, 1st edn, 2015.

149 D. Tan, Y. Li, F. Qi, H. Yang, Q. Gong, X. Dong and X. Duan, *Appl. Phys. Lett.*, 2007, **90**, 071106.

150 Y. Bougdid, Y. E. Idrissi, I. Maouli and Z. Sekkat, *Molecular and Nano Machines II*, SPIE, 2019, vol. 11098, pp. 8–16.

151 D. Serien and K. Sugioka, *ACS Biomater. Sci. Eng.*, 2020, **6**, 1279–1287.

152 A. Nakayama, Y. Kumamoto, A. Taguchi and K. Fujita, *Advanced Fabrication Technologies for Micro/Nano Optics and Photonics XV*, SPIE, 2022, vol. 12012, pp. 7–10.

153 S. W. Hell and J. Wichmann, *Opt. Lett.*, 1994, **19**, 780–782.

154 C. Barner-Kowollik, M. Bastmeyer, E. Blasco, G. Delaittre, P. Müller, B. Richter and M. Wegener, *Angew. Chem., Int. Ed.*, 2017, **56**, 15828–15845.

155 T. A. Klar, R. Wollhofen and J. Jacak, *Phys. Scr.*, 2014, 014049.

156 P. Somers, A. Münchinger, S. Maruo, C. Moser, X. Xu and M. Wegener, *Nat. Rev. Phys.*, 2024, **6**, 99–113.

157 M. He, Z. Zhang, C. Cao, G. Zhou, C. Kuang and X. Liu, *Laser Photonics Rev.*, 2022, **16**, 2100229.

158 S. H. Park, T. W. Lim, D.-Y. Yang, R. H. Kim and K.-S. Lee, *Macromol. Res.*, 2006, **14**, 559–564.

159 K. Takada, H.-B. Sun and S. Kawata, *Appl. Phys. Lett.*, 2005, **86**, 071122.

160 I. Sakellari, E. Kabouraki, D. Gray, V. Purlys, C. Fotakis, A. Pikulin, N. Bityurin, M. Vamvakaki and M. Farsari, *ACS Nano*, 2012, **6**, 2302–2311.

161 D. Wu, S.-Z. Wu, L.-G. Niu, Q.-D. Chen, R. Wang, J.-F. Song, H.-H. Fang and H.-B. Sun, *Appl. Phys. Lett.*, 2010, **97**, 031109.

162 D. Wu, Q.-D. Chen, L.-G. Niu, J. Jiao, H. Xia, J.-F. Song and H.-B. Sun, *IEEE Photonics Technol. Lett.*, 2009, **21**, 1535–1537.

163 C. R. K. Marrian and D. M. Tennant, *J. Vac. Sci. Technol., A*, 2003, **21**, S207–S215.

164 M. Malinauskas, A. Žukauskas, S. Hasegawa, Y. Hayasaki, V. Mizeikis, R. Buividas and S. Juodkazis, *Light: Sci. Appl.*, 2016, **5**, e16133.

165 F. Cantoni, D. Maher, E. Bosler, S. Kühne, L. Barbe, D. Oberschmidt, C. Marquette, R. Taboryski, M. Tenje and A.-I. Bunea, *Addit. Manuf.*, 2023, **76**, 103761.

166 T. Koch, W. Zhang, T. T. Tran, Y. Wang, A. Mikitisin, J. Puchhammer, J. R. Greer, A. Ovsianikov, F. Chalupa-Gantner and M. Lunzer, *Adv. Mater.*, 2024, **36**, 2308497.

167 M. Malinauskas, A. Žukauskas, K. Belazaras, K. Tikuišis, V. Purlys, R. Gadonas and A. Piskarskas, *Eur. Phys. J.: Appl. Phys.*, 2012, **58**, 20501.

168 M. Luitz, B. M. Kırpat Konak, A. Sherbaz, R. Prediger, N. Nekoonam, B. Di Ventura, F. Kotz-Helmer and B. E. Rapp, *Adv. Mater. Technol.*, 2023, **8**, 2300667.

169 E. Skliutas, G. Merkininkaitė, S. Maruo, W. Zhang, W. Chen, W. Deng, J. Greer, G. von Freymann and M. Malinauskas, *Nat. Rev. Methods Primer*, 2025, **5**, 15.

170 H. Schift, *J. Vac. Sci. Technol., B: Microelectron. Nanometer Struct. Process., Meas., Phenom.*, 2008, **26**, 458–480.

171 D. Gonzalez-Hernandez, S. Varapnickas, A. Bertoncini, C. Liberale and M. Malinauskas, *Adv. Opt. Mater.*, 2023, **11**, 2201701.

172 H. Wang, C.-F. Pan, C. Li, K. S. Menghrajani, M. A. Schmidt, A. Li, F. Fan, Y. Zhou, W. Zhang, H. Wang, P. N. S. Nair, J. Y. E. Chan, T. Mori, Y. Hu, G. Hu, S. A. Maier, H. Ren, H. Duan and J. K. W. Yang, *Int. J. Extreme Manuf.*, 2024, **6**, 042002.

173 Z.-C. Ma, X.-Y. Hu, Y.-L. Zhang, X.-Q. Liu, Z.-S. Hou, L.-G. Niu, L. Zhu, B. Han, Q.-D. Chen and H.-B. Sun, *Adv. Funct. Mater.*, 2019, **29**, 1903340.

174 B. Li, C. Liao, Z. Cai, J. Zhou, C. Zhao, L. Jing, J. Wang, C. Xiong, L. Xu, Y. Wang and Y. Wang, *Fundam. Res.*, 2024, **4**, 123–130.

175 T. Gissibl, S. Thiele, A. Herkommer and H. Giessen, *Nat. Commun.*, 2016, **7**, 11763.

176 S. Thiele, K. Arzenbacher, T. Gissibl, H. Giessen and A. M. Herkommer, *Sci. Adv.*, 2017, **3**, e1602655.

177 A. Kubec, M.-C. Zdora, U. T. Sanli, A. Diaz, J. Vila-Comamala and C. David, *Nat. Commun.*, 2022, **13**, 1305.

178 U. T. Sanli, G. Rodgers, M.-C. Zdora, P. Qi, J. Garrevoet, K. V. Falch, B. Müller, C. David and J. Vila-Comamala, *Light: Sci. Appl.*, 2023, **12**, 107.

179 H. Ren, J. Jang, C. Li, A. Aigner, M. Plidschun, J. Kim, J. Rho, M. A. Schmidt and S. A. Maier, *Nat. Commun.*, 2022, **13**, 4183.

180 F. Balli, M. A. Sultan, A. Ozdemir and J. T. Hastings, *Nanophotonics*, 2021, **10**, 1259–1264.

181 A. Bogucki, L. Zinkiewicz, M. Grzeszczyk, W. Pacuski, K. Nogajewski, T. Kazimierczuk, A. Rodek, J. Suffczyński, K. Watanabe, T. Taniguchi, P. Wasylczyk, M. Potemski and P. Kossacki, *Light: Sci. Appl.*, 2020, **9**, 48.

182 Y. Tao, C. Wei, J. Liu, C. Deng, S. Cai and W. Xiong, *Nanoscale*, 2019, **11**, 9176–9184.

183 X. Zhou, X. Liu and Z. Gu, *Adv. Mater.*, 2024, **36**, 2409326.

184 U. Staudinger, G. Zyla, B. Krause, A. Janke, D. Fischer, C. Esen, B. Voit and A. Ostendorf, *Microelectron. Eng.*, 2017, **179**, 48–55.

185 K. Kurselis, R. Kiyan, V. N. Bagratashvili, V. K. Popov and B. N. Chichkov, *Opt. Express*, 2013, **21**, 31029–31035.

186 Q. Guo, S. Xiao, A. Aumann, M. Jaeger, M. Chakif, R. Ghadiri, C. Esen, M. Ma and A. Ostendorf, *J. Laser Micro/Nanoeng.*, 2024, **7**, 44.

18628 | *J. Mater. Chem. C*, 2025, **13**, 18597–18630

This journal is © The Royal Society of Chemistry 2025

187 S. Gong, Z. H. Zhu and S. A. Meguid, *Polymer*, 2015, **56**, 498–506.

188 H. Yang, B. Fu, D. Li, Y. Tian, Y. Chen, M. Mattila, Z. Yong, R. Li, A. Hassanien, C. Yang, I. Tittonen, Z. Ren, J. Bai, Q. Li, E. I. Kauppinen, H. Lipsanen and Z. Sun, *Nanoscale*, 2015, **7**, 11199–11205.

189 C. Rutherglen, D. Jain and P. Burke, *Nat. Nanotechnol.*, 2009, **4**, 811–819.

190 H. Shi, L. Ding, D. Zhong, J. Han, L. Liu, L. Xu, P. Sun, H. Wang, J. Zhou, L. Fang, Z. Zhang and L.-M. Peng, *Nat. Electron.*, 2021, **4**, 405–415.

191 O. Dadras-Toussi, M. Khorrami, A. S. C. Louis Sam Titus, S. Majd, C. Mohan and M. R. Abidian, *Adv. Mater.*, 2022, **34**, 2200512.

192 G. Tiwari and R. Tiwari, *Pharm. Methods*, 2010, **1**, 25–38.

193 J. Liu, Y. Liu, C. Deng, K. Yu, X. Fan, W. Zhang, Y. Tao, H. Hu, L. Deng and W. Xiong, *Adv. Mater. Technol.*, 2022, **7**, 2101230.

194 C. Soci, A. Zhang, B. Xiang, S. A. Dayeh, D. P. R. Aplin, J. Park, X. Y. Bao, Y. H. Lo and D. Wang, *Nano Lett.*, 2007, **7**, 1003–1009.

195 B. D. Boruah, *Nanoscale Adv.*, 2019, **1**, 2059–2085.

196 J. Long, W. Xiong, C. Wei, C. Lu, R. Wang, C. Deng, H. Liu, X. Fan, B. Jiao, S. Gao and L. Deng, *Nano Lett.*, 2020, **20**, 5159–5166.

197 A. Aghakhani, O. Yasa, P. Wrede and M. Sitti, *Proc. Natl. Acad. Sci. U. S. A.*, 2020, **117**, 3469–3477.

198 Y. Xiao, J. Zhang, B. Fang, X. Zhao and N. Hao, *Micromachines*, 2022, **13**, 481.

199 A.-I. Bunea, D. Martella, S. Nocentini, C. Parmeggiani, R. Taboryski and D. S. Wiersma, *Adv. Intell. Syst.*, 2021, **3**, 2000256.

200 S. Koo, *Appl. Sci.*, 2020, **10**, 8563.

201 C. Zheng, F. Jin, Y. Zhao, M. Zheng, J. Liu, X. Dong, Z. Xiong, Y. Xia and X. Duan, *Sens. Actuators, B*, 2020, **304**, 127345.

202 S. Palagi and P. Fischer, *Nat. Rev. Mater.*, 2018, **3**, 113–124.

203 M. Sitti, *Nat. Rev. Mater.*, 2018, **3**, 74–75.

204 Z. Lao, N. Xia, S. Wang, T. Xu, X. Wu and L. Zhang, *Micromachines*, 2021, **12**, 465.

205 F. Soto and R. Chrostowski, *Front. Bioeng. Biotechnol.*, 2018, **6**, 170.

206 F. Qiu, S. Fujita, R. Mhanna, L. Zhang, B. R. Simona and B. J. Nelson, *Adv. Funct. Mater.*, 2015, **25**, 1666–1671.

207 L. Zhang, T. Petit, K. E. Peyer and B. J. Nelson, *Nanomedicine*, 2012, **8**, 1074–1080.

208 M. Hoop, F. Mushtaq, C. Hurter, X.-Z. Chen, B. J. Nelson and S. Pané, *Nanoscale*, 2016, **8**, 12723–12728.

209 X.-Z. Chen, M. Hoop, N. Shamsudhin, T. Huang, B. Özkale, Q. Li, E. Siringil, F. Mushtaq, L. Di Tizio, B. J. Nelson and S. Pané, *Adv. Mater.*, 2017, **29**, 1605458.

210 A. Chałupniak, E. Morales-Narváez and A. Merkoçi, *Adv. Drug Delivery Rev.*, 2015, **95**, 104–116.

211 S. Guo, Q. Pan and M. B. Khamesee, *Microsyst. Technol.*, 2008, **14**, 307–314.

212 F. Qiu and B. J. Nelson, *Engineering*, 2015, **1**, 021–026.

213 B. J. Nelson, I. K. Kaliakatsos and J. J. Abbott, *Annu. Rev. Biomed. Eng.*, 2010, **12**, 55–85.

214 B. Gaihre, M. S. Khil, D. R. Lee and H. Y. Kim, *Int. J. Pharm.*, 2009, **365**, 180–189.

215 X. Wang, X.-H. Qin, C. Hu, A. Terzopoulou, X.-Z. Chen, T.-Y. Huang, K. Maniura-Weber, S. Pané and B. J. Nelson, *Adv. Funct. Mater.*, 2018, **28**, 1804107.

216 X. Wang, C. Hu, L. Schurz, C. De Marco, X. Chen, S. Pané and B. J. Nelson, *ACS Nano*, 2018, **12**, 6210–6217.

217 F. Qiu, L. Zhang, K. E. Peyer, M. Casarosa, A. Franco-Obregón, H. Choi and B. J. Nelson, *J. Mater. Chem. B*, 2013, **2**, 357–362.

218 Y. Tu, F. Peng, P. B. White and D. A. Wilson, *Angew. Chem., Int. Ed.*, 2017, **56**, 7620–7624.

219 M. Dong, X. Wang, X.-Z. Chen, F. Mushtaq, S. Deng, C. Zhu, H. Torlakcik, A. Terzopoulou, X.-H. Qin, X. Xiao, J. Puigmartí-Luis, H. Choi, A. P. Pêgo, Q.-D. Shen, B. J. Nelson and S. Pané, *Adv. Funct. Mater.*, 2020, **30**, 1910323.

220 H. Ceylan, I. C. Yasa, O. Yasa, A. F. Tabak, J. Giltinan and M. Sitti, *ACS Nano*, 2019, **13**, 3353–3362.

221 F. Striggow, M. Medina-Sánchez, G. K. Auernhammer, V. Magdanz, B. M. Friedrich and O. G. Schmidt, *Small*, 2020, **16**, 2000213.

222 L. Schwarz, M. Medina-Sánchez and O. G. Schmidt, *Reproduction*, 2020, **159**, R83–R96.

223 L. Fortuna and A. Buscarino, *Micromachines*, 2022, **13**, 1207.

224 J.-D. Kim, S.-U. Hwang and Y.-G. Lee, *J. Micromech. Microeng.*, 2012, **22**, 105003.

225 J. Köhler, S. I. Ksouri, C. Esen and A. Ostendorf, *Microsyst. Nanoeng.*, 2017, **3**, 1–7.

226 S. Maruo, A. Takaura and Y. Saito, *Opt. Express*, 2009, **17**, 18525–18532.

227 C. Xin, D. Jin, Y. Hu, L. Yang, R. Li, L. Wang, Z. Ren, D. Wang, S. Ji, K. Hu, D. Pan, H. Wu, W. Zhu, Z. Shen, Y. Wang, J. Li, L. Zhang, D. Wu and J. Chu, *ACS Nano*, 2021, **15**, 18048–18059.

228 E. Avci, M. Grammatikopoulou and G.-Z. Yang, *Adv. Opt. Mater.*, 2017, **5**, 1700031.

229 S. Armon, E. Efrati, R. Kupferman and E. Sharon, *Science*, 2011, **333**, 1726–1730.

230 A. Ghosh, C. Yoon, F. Ongaro, S. Scheggi, F. M. Selaru, S. Misra and D. H. Gracias, *Front. Mech. Eng.*, 2017, **3**, 7.

231 Y. Kim, H. Yuk, R. Zhao, S. A. Chester and X. Zhao, *Nature*, 2018, **558**, 274–279.

232 C. Xin, L. Yang, J. Li, Y. Hu, D. Qian, S. Fan, K. Hu, Z. Cai, H. Wu, D. Wang, D. Wu and J. Chu, *Adv. Mater.*, 2019, **31**, 1808226.

233 B. Esteban-Fernández de Ávila, P. Angsantikul, D. E. Ramírez-Herrera, F. Soto, H. Teymourian, D. Dehaini, Y. Chen, L. Zhang and J. Wang, *Sci. Rob.*, 2018, **3**, eaat0485.

234 K. Wei, C. Tang, H. Ma, X. Fang and R. Yang, *Biomater. Sci.*, 2024, **12**, 4301–4334.

235 W. Zhu, J. Li, Y. J. Leong, I. Rozen, X. Qu, R. Dong, Z. Wu, W. Gao, P. H. Chung, J. Wang and S. Chen, *Adv. Mater.*, 2015, **27**, 4411–4417.

This journal is © The Royal Society of Chemistry 2025

J. Mater. Chem. C, 2025, **13**, 18597–18630 | **18629**

236 T. Xu, J. Zhang, M. Salehizadeh, O. Onaizah and E. Diller, *Sci. Rob.*, 2019, **4**, eaav4494.

237 M. McCandless, A. Perry, N. DiFilippo, A. Carroll, E. Billatos and S. Russo, *Soft Robot.*, 2022, **9**, 754–766.

238 H. C. Lee, N. Elder, M. Leal, S. Stantial, E. Vergara Martinez, S. Jos, H. Cho and S. Russo, *Nat. Commun.*, 2024, **15**, 8456.

239 D. Van Lewen, T. Janke, H. Lee, R. Austin, E. Billatos and S. Russo, *Adv. Intell. Syst.*, 2023, **5**, 2200326.

240 M. Sitti, H. Ceylan, W. Hu, J. Giltinan, M. Turan, S. Yim and E. Diller, *Proc. IEEE*, 2015, **103**, 205–224.

241 G. Thalhammer, R. Steiger, M. Meinschad, M. Hill, S. Bernet and M. Ritsch-Marte, *Biomed. Opt. Express*, 2011, **2**, 2859–2870.

242 S. Hu and D. Sun, *Int. J. Rob. Res.*, 2011, **30**, 1681–1694.

243 Y. Zhang, C. Min, X. Dou, X. Wang, H. P. Urbach, M. G. Somekh and X. Yuan, *Light: Sci. Appl.*, 2021, **10**, 59.

244 D. Gao, W. Ding, M. Nieto-Vesperinas, X. Ding, M. Rahman, T. Zhang, C. Lim and C.-W. Qiu, *Light: Sci. Appl.*, 2017, **6**, e17039.

245 A. G. Banerjee, S. Chowdhury, S. K. Gupta and W. Losert, *J. Biomed. Opt.*, 2011, **16**, 051302.

246 H. Maruyama, R. Iitsuka, K. Onda and F. Arai, *IEEE Int. Conf. Rob. Autom.*, 2010, 482–487.

247 Y. Tan, C. Kong, S. Chen, S. H. Cheng, R. A. Li and D. Sun, *J. Biomech.*, 2012, **45**, 123–128.

248 M. J. Villangca, D. Palima, A. R. Bañas and J. Glückstad, *Light: Sci. Appl.*, 2016, **5**, e16148.

249 L. Zhang, C. Wang, C. Zhang, Y. Xue, L. Ye, L. Xu, Y. Hu, J. Li, J. Chu and D. Wu, *Nano Lett.*, 2024, **24**, 2671–2679.

250 Q. Geng, D. Wang, P. Chen and S.-C. Chen, *Nat. Commun.*, 2019, **10**, 2179.

251 W. Ouyang, X. Xu, W. Lu, N. Zhao, F. Han and S.-C. Chen, *Nat. Commun.*, 2023, **14**, 1716.

252 P. Somers, S. Koch, P. Kiefer, M. L. Meretska and M. Wegener, *Opt. Mater. Express*, 2024, **14**, 2370–2376.

253 T. Liu, P. Tao, X. Wang, H. Wang, M. He, Q. Wang, H. Cui, J. Wang, Y. Tang, J. Tang, N. Huang, C. Kuang, H. Xu and X. He, *Nat. Nanotechnol.*, 2024, **19**, 51–57.

254 L. Siegle, S. Ristok and H. Giessen, *Opt. Express*, 2023, **31**, 4179–4189.

255 T. Aderneuer, O. Fernández and R. Ferrini, *Opt. Express*, 2021, **29**, 39511–39520.

256 D. Perevoznik, R. Nazir, R. Kiyan, K. Kurselis, B. Koszarna, D. T. Gryko and B. N. Chichkov, *Opt. Express*, 2019, **27**, 25119–25125.

257 G. Zyla, N. Surkamp, E. L. Gurevich, C. Esen, A. Klehr, A. Knigge, M. R. Hofmann and A. Ostendorf, *Opt. Lett.*, 2020, **45**, 4827–4830.

258 V. Hahn, P. Rietz, F. Hermann, P. Müller, C. Barner-Kowollik, T. Schlöder, W. Wenzel, E. Blasco and M. Wegener, *Nat. Photonics*, 2022, **16**, 784–791.

259 F. Mayer, S. Richter, J. Westhauser, E. Blasco, C. Barner-Kowollik and M. Wegener, *Sci. Adv.*, 2019, **5**, eaau9160.

260 L. Yang, F. Mayer, U. H. F. Bunz, E. Blasco and M. Wegener, *Light Adv. Manuf.*, 2021, **2**, 296–312.

261 Y. Yang, V. A. Kelkar, H. S. Rajput, A. C. Salazar Coariti, K. C. Toussaint and C. Shao, *J. Manuf. Process.*, 2022, **76**, 841–849.

262 N. Lang, S. Enns, J. Hering and G. von Freymann, *Opt. Express*, 2022, **30**, 28805–28816.

263 R. Pingali and S. K. Saha, *J. Micro Nano-Manuf.*, 2022, **10**, 03100.

264 T. Alletzhäusser, R. Zvagelsky, S. Kalt, P. Friederich and M. Wegener, *Laser 3D Manufacturing XII*, SPIE, 2025, vol. PC13354, p. PC1335403.

18630 | *J. Mater. Chem. C*, 2025, **13**, 18597–18630

This journal is © The Royal Society of Chemistry 2025